

Occamy: A 432-Core Dual-Chiplet Dual-HBM2E 768-DP-GFLOP/s RISC-V System for 8-to-64-bit Dense and Sparse Computing in 12nm FinFET

Paul Scheffler^{✉*}, Graduate Student Member (GSM), IEEE, Thomas Benz^{✉*}, GSM, IEEE, Viviane Potocnik[✉], GSM, IEEE, Tim Fischer[✉], GSM, IEEE, Luca Colagrande[✉], GSM, IEEE, Nils Wistoff[✉], GSM, IEEE, Yichao Zhang[✉], GSM, IEEE, Luca Bertaccini[✉], GSM, IEEE, Gianmarco Ottavi[✉], GSM, IEEE, Manuel Eggimann[✉], Member, IEEE, Matheus Cavalcante[✉], Member, IEEE, Gianna Paulin[✉], Member, IEEE, Frank K. Gürkaynak[✉], Davide Rossi[✉], Senior Member, IEEE, and Luca Benini[✉], Fellow, IEEE

Abstract—ML and HPC applications increasingly combine dense and sparse memory access computations to maximize storage efficiency. However, existing CPUs and GPUs struggle to flexibly handle these heterogeneous workloads with consistently high compute efficiency. We present Occamy, a 432-Core, 768-DP-GFLOP/s, dual-HBM2E, dual-chiplet RISC-V system with a latency-tolerant hierarchical interconnect and in-core streaming units (SUs) designed to accelerate dense and sparse FP8-to-FP64 ML and HPC workloads. We implement Occamy’s compute chiplets in 12nm FinFET, and its passive interposer, Hedwig, in a 65 nm node. On dense linear algebra (LA), Occamy achieves a competitive FPU utilization of 89%. On stencil codes, Occamy reaches an FPU utilization of 83% and a technology-node-normalized compute density of 11.1 DP-GFLOP/s/mm², leading state-of-the-art (SoA) processors by 1.7× and 1.2×, respectively. On sparse-dense linear algebra (LA), it achieves 42% FPU utilization and a normalized compute density of 5.95 DP-GFLOP/s/mm², surpassing the SoA by 5.2× and 11×, respectively. On, sparse-sparse LA, Occamy reaches a throughput of up to 187 GCOMP/s at 17.4 GCOMP/s/W and a compute density of 3.63 GCOMP/s/mm². Finally, we reach up to 75% and 54% FPU utilization on dense (LLM) and graph-sparse (GCN) ML inference workloads. Occamy’s RTL is freely available under a permissive open-source license.

Index Terms—2.5D Integration, Chiplet, Interposer, RISC-V, Manycore, Machine Learning, High-Performance Computing, Sparse Acceleration, Stencil Acceleration, Multi-Precision.

I. INTRODUCTION

Surging performance needs and large, sparse models in machine learning (ML) and high-performance computing (HPC) push data-driven workloads toward a mixture of sparse and dense computations. In ML, the sparsification of dense models significantly reduces both their computational and memory footprints [1], and the recent proliferation of >100B-parameter transformers has reinvigorated sparsification efforts to address

severe memory capacity bottlenecks [2], [3]. In HPC, applications like multiphysics simulation and graph analytics heavily rely on sparse linear algebra (LA), stencil computations, and graph pattern matching to handle large, high-dimensional problems [4].

Large-scale ML and HPC applications traditionally target manycore CPUs and GPUs whose parallel datapaths achieve high ($\geq 75\%$) FPU utilization and energy efficiency on dense workloads [5], [6]. However, these general-purpose architectures struggle with the indirect address computations, irregular memory access patterns, and computational imbalance inherent to sparse workloads. Consequently, they achieve peak FPU utilizations of less than 50% on stencil codes [7]–[9] and less than 10% on sparse LA [6], [10]–[12]. While hardware accelerators for sparse computation have been proposed, they usually target narrow, domain-specific sparsity regimes: accelerators for ML [13]–[16] support low-precision data formats (≤ 16 b) and low ($\leq 80\%$) or structured sparsity, while more generic sparse LA [17]–[20] and tensor algebra [21] accelerators often target specific operators [17]–[20] or dataflows [17], [18]. General-purpose acceleration solutions based on coarse-grained reconfigurable arrays (CGRAs) [22], [23] or instruction set architecture (ISA) extensions [24]–[29] are more flexible, but they have not yet been demonstrated on silicon at scale [22], [24]–[29] or tackle only one- [24]–[27] or two-sided sparsity [28], [29]. Hence, there is a lack of *silicon-proven* processors that efficiently handle the diverse sparse compute requirements of current ML and HPC without compromising on dense compute performance.

We present *Occamy*, a 432-core, 768-DP-GFLOP/s dual-chiplet RISC-V system whose architecture is specifically designed to flexibly handle both dense and sparse ML and HPC workloads with high FPU utilization and energy efficiency. Unlike existing hardware targeting sparse compute, Occamy is designed for *general-purpose* sparse acceleration and avoids specialization to specific workloads, sparsity patterns, and value densities. Each Occamy chiplet features 24 compute *clusters*, a Linux-capable host, 16 GiB of HBM2E DRAM, and a fully digital die-to-die (D2D) link. In each cluster, nine cores share an explicitly managed 128 KiB scratchpad memory (SPM); eight *worker* cores with SIMD-capable FPUs [30]

* Authors contributed equally to this research.

P. Scheffler, T. Benz, V. Potocnik, T. Fischer, L. Colagrande, N. Wistoff, Y. Zhang, L. Bertaccini, F. K. Gürkaynak, and L. Benini are with the Integrated Systems Laboratory (IIS), ETH Zurich, Switzerland (email: paulsc@ethz.ch). G. Ottavi, D. Rossi, and L. Benini are with the Department of Electrical, Electronic and Information Engineering (DEI), University of Bologna, Italy. M. Eggimann and G. Paulin are with Axelera AI. M. Cavalcante is with the Robust Systems Group (RSG) at the Computer Systems Laboratory (CSL) of Stanford University, CA, USA.

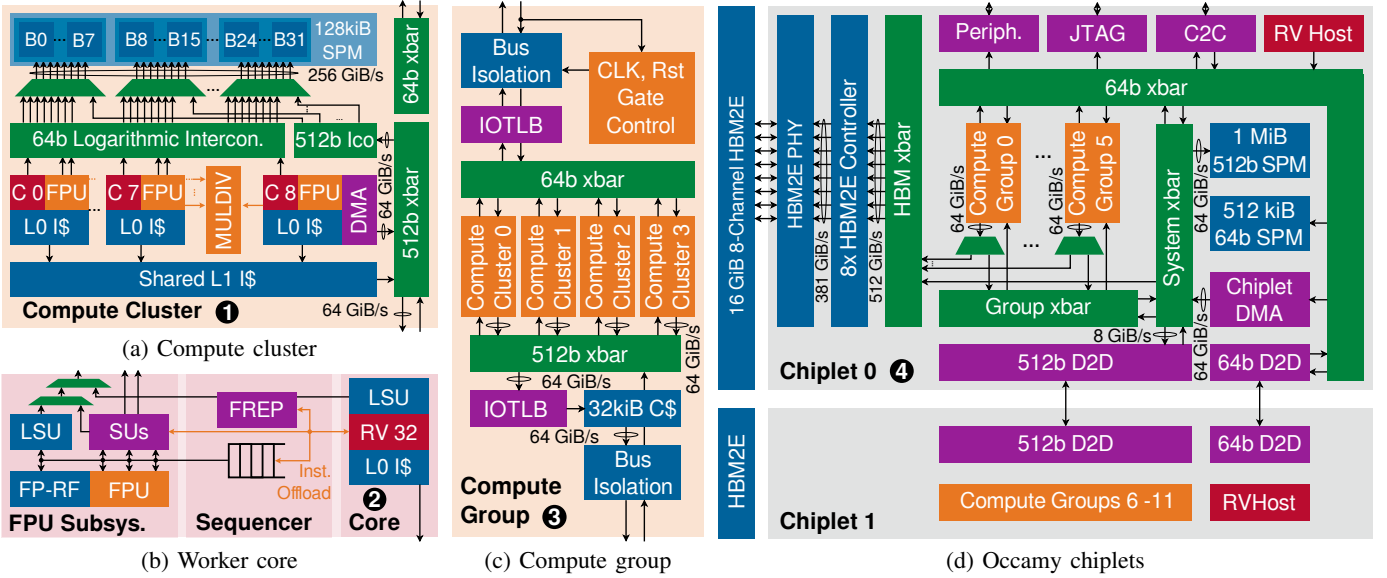


Fig. 1: Hierarchical architecture of the two Occamy compute chiplets including the two HBM2E interfaces and D2D link.

are kept busy by sparsity-capable streaming units (SUs) [31], while an additional *DMA control* core [32] enables latency-tolerant transfers of large data tiles to or from the SPM. The hierarchical chiplet interconnect provides a 512-bit network for bulk data transfers and a 64-bit network for message passing and synchronization.

We implemented Occamy’s 73 mm² compute chiplets in GlobalFoundries’ 12 nm LP+ technology and its passive interposer named *Hedwig* in a 65 nm node. On dense workloads, Occamy achieves competitive FPU utilizations of up to 89%. Executing stencil codes, we reach FPU utilizations of up to 83% and a technology-node-normalized compute density of up to 11.1 DP-GFLOP/s/mm², leading state-of-the-art processors by 1.7 \times and 1.2 \times , respectively. On sparse-dense LA, we achieve up to 42% FPU utilization and a node-normalized compute density of up to 5.95 DP-GFLOP/s/mm², substantially surpassing the state-of-the-art (SoA) by 5.2 \times and 11 \times , respectively. We further achieve a sparse-sparse LA throughput of up to 187 GCOMP/s at an energy efficiency of 17.4 GCOMP/s/W and a compute density of 3.63 GCOMP/s/mm². Finally, we reach FPU utilizations of up to 75% and 54% on GPT-J inference and a graph convolutional network (GCN) layer, respectively. To the best of our knowledge, Occamy is the first open-source multi-chiplet RISC-V manycore demonstrated in silicon; the register transfer level (RTL) description of its digital core, including the compute groups, hierarchical interconnect, and D2D link, is freely available under a permissive open-source license¹.

This paper extends our previous work [33], significantly elaborating on Occamy’s architecture, its programming model, and its silicon implementation. We further add new measurement results on dense LA workloads, FP8-to-FP64 SIMD computation, ML inference applications, and our D2D link and extend our state-of-the-art comparison with additional related works and metrics.

The remainder of the paper is organized as follows. Section II presents Occamy’s hierarchical compute chiplet architecture. In Section III, we illustrate how Occamy, its SUs, and its asynchronous DMA engines are programmed to achieve high compute efficiency. Section IV describes how the Occamy chiplets, the Hedwig interposer, and the carrier board were implemented. Section V presents our experimental results. In Section VI, we discuss how Occamy compares to SoA CPUs and GPUs as well as existing sparse acceleration proposals. Finally, we provide a conclusion in Section VII.

II. ARCHITECTURE

Occamy combines two 216-core compute chiplets on a passive interposer, each paired with an eight-device, 16 GiB HBM2E stack and connected through a fully digital, fault-tolerant D2D link. Figure 1 shows the hierarchical compute chiplet architecture, which we describe in a bottom-up fashion in the following sections.

A. Compute Cluster

Occamy’s compute cores are based on the RV32G ISA and are organized into compute *clusters* ① [34] shown in Figure 1a. Within each cluster, eight worker cores and one DMA control core share a 128 KiB 32-bank SPM through a single-cycle logarithmic interconnect with double-word interleaving. The clusters also feature 8 KiB of shared L1 instruction cache, a shared integer multiply-divide unit, a local hardware synchronization barrier, and 16 retargetable performance counters capable of tracking various per-core and cluster-wide events.

Each worker core ②, shown in Figure 1b, features a 64-bit-wide SIMD FPU supporting FP64, FP32, FP16, FP16alt (8,7), FP8, and FP8alt (4,3) formats. In addition to fused multiply-accumulate (FMA) instructions, the FPU supports widening sum-dot-product and three-addend summation instructions for all FP8 and FP16 formats [30]. Two worker-core ISA extensions maximize the FPU utilization for both regular and

¹<https://github.com/pulp-platform/occamy>

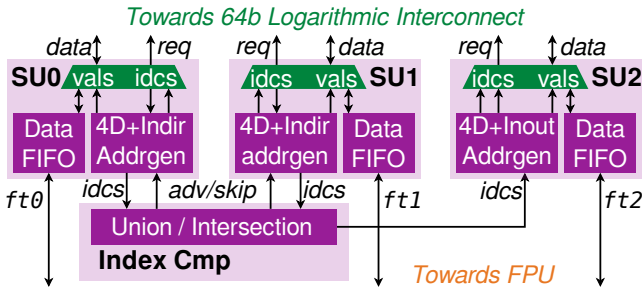


Fig. 2: Architecture and interconnection of the three cooperating sparsity-capable SUs in each worker core.

irregular workloads: a hardware loop buffer [34] and three sparsity-capable SUs [31].

The SUs, shown in Figure 2, map buffered streams of SPM accesses directly to floating-point registers, generating the necessary addresses in hardware. All three SUs in each core support up to 4D strided accesses to accelerate dense tensor workloads; for instance, the general matrix multiply (GEMM) used in our later evaluation in Section V-B utilizes all four SU loop levels to cover the algorithm’s three nested loops and an inner unroll for performance. Two SUs additionally support indirect streams with 8-, 16-, or 32-bit indices to accelerate the scatter-gather accesses underlying irregular-access applications such as sparse-dense LA and stencil codes. Finally, these indirect SUs can also compare their indices to accelerate the sparse tensor intersection and union underlying sparse-sparse LA or graph matching; the third SU can optionally write out the joint indices for sparse result tensors. Our SUs can handle any sparse tensor format whose major axis is given by a value-index array pair, which includes the widespread and scalable CSR, CSC, CSF, and many of their variations, without restrictive assumptions on operand structure or density. In general, our SUs enable a sustained per-core bandwidth of up to three double-words per cycle into the shared SPM. We will discuss in detail how SUs are programmed and leveraged for dense and sparse workload acceleration in Section III-A.

The cluster SPM is dimensioned to balance throughput, interconnect complexity, and area. 32 banks are chosen to reduce the probability of banking conflicts between SUs (24 per cluster) while keeping the logarithmic interconnect physically implementable. A capacity of 128 KiB achieves a reasonable SRAM bit density (avoiding significant drops that would appear for ≤ 4 KiB banks) while keeping area prevalently allocated to compute logic.

The DMA control core in each cluster features a tightly-coupled 512-bit DMA engine [32], enabling asynchronous $\leq 2D$ transfers between external memory (other clusters, HBM2E, or other chiplet) and the local SPM. This core coordinates the computation of worker cores and their fine-grained, low-latency accesses to the SPM with the latency-tolerant DMA transfers of large, double-buffered data tiles to and from the SPM. The DMA engine accesses blocks of eight SPM banks (*superbanks*) at once through a secondary interconnect, transferring up to 64 B per cycle or 64 GiB/s; this way, it maximizes throughput without significantly slowing down ongoing memory-intensive computations, which can

access up to 24 SPM banks at once using all SUs. To reduce backpressure in the group- and chiplet-level interconnect, the DMA has priority accessing the SPM through the secondary interconnect over the cores and SUs. We will elaborate on the DMA engine’s programming model and its use in double-buffered data tiling in Section III-B.

B. Compute Group

Four clusters together form the next compute hierarchy level, a *group* ③, shown in Figure 1c. Clusters within a group have full-bandwidth access to each other through two fully connected advanced eXtensible interface 4 (AXI4) crossbars: a 512-bit crossbar used by DMA engines and instruction caches for bulk transfers and an atomics-capable 64-bit crossbar used by cores for global synchronization and message passing. Thus, groups allow their clusters to locally share data at higher bandwidths than at the global level and constitute a replicable multi-cluster design that significantly simplifies top-level chiplet implementation.

On each crossbar, a group has one outgoing and one incoming port, providing a shared bandwidth to and from the chiplet interconnect of 64 GiB/s for bulk transfers and 8 GiB/s for message passing. Providing one outgoing port per group best matches the HBM2E bandwidth available at the chiplet level and keeps the chiplet-level interconnect implementable. IO translation lookaside buffers (IOTLBs) on the outgoing ports allow for per-group address remapping and access control at page granularity. A remappable 32 KiB constant cache on the outgoing 512-bit port can be used to cache program code and other immutable data. Finally, the groups can be individually clock-gated, reset, and isolated from their interconnect ports to the chiplet level through memory-mapped registers for online power management.

C. Occamy Chiplets

Figure 1d shows Occamy’s top-level chiplet architecture ④. Each chiplet features six groups, totaling 216 cores, and a single Linux-capable 64-bit RISC-V host processor managing the groups and all other on-chip resources. Like the groups, the chiplets feature a hierarchical 512-bit AXI4 network for bulk data transfers and an atomics-capable 64-bit AXI4 network for synchronization, message passing, and management. The D2D link, which serializes cross-chiplet transactions, comprises a *narrow* and a *wide* segment carrying 64-bit and 512-bit transactions, respectively.

The 512-bit network is composed of three fully connected crossbars. Each group’s 64 GiB/s outgoing port provides access to an *HBM* crossbar and a *group* crossbar, interconnecting the six on-chip groups. The *HBM* crossbar provides access to the eight on-chip 47.68 GiB/s HBM2E controllers (381.47 GiB/s in total). It can be configured at runtime to interleave the HBM2E channels at page granularity, facilitating load balancing and data reuse. A *system* crossbar connects the group and HBM crossbars to the wide D2D segment and 64-bit network, providing all actors across both chiplets access to the entire memory space. It also connects to a 1 MiB SPM used for low-latency on-chip storage of shared data and a

chiplet-level DMA engine used by the host for fast, explicit data movement and memory initialization. As a chiplet-level memory, the 1 MiB SPM was dimensioned to be significantly larger than the 128 KiB cluster SPMs, but small enough to fit into the area available to chiplet-level logic and routing.

The 64-bit network consists of a single crossbar. It connects the Linux-capable host and the 64-bit ports of the groups to the narrow D2D segment, the 512-bit network, and various peripherals. It also features a 512 KiB SPM used by the host for management tasks. The peripherals include UART, I2C, QSPI, GPIOs, a 1.33 Gb/s off-interposer chip-to-chip (C2C) link, and a JTAG test access point for live host processor debugging. They also include RISC-V-compliant timers and platform-level interrupt controllers providing interrupts for both the host processor and all on-chip compute cores.

The main benefit of our hierarchical crossbar-based interconnect over a ring or mesh topology is its *symmetry*: the memory topology looks identical to all compute cores and clusters, meaning that the architectural bandwidth and latency of accesses to each hierarchy level (cluster, group, chiplet) are *constant*. This greatly simplifies programming, as network performance is homogeneous and code can be written in a *cluster-agnostic* way without sacrificing performance. However, crossbars pose challenges in physical implementation, requiring effort to provision sufficient bandwidth while managing area costs. While this was feasible for our design, larger systems may face scalability limitations. In this case, alternative network-on-chip (NoC) topologies such as mesh and torus could be more suitable.

The D2D link enables seamless communication across chiplets, allowing the system to scale to 432 cores and two HBM2E stacks. This approach improves overall performance while avoiding the yield challenges and high manufacturing costs associated with large monolithic dies [35]. The D2D link consists of a narrow segment, optimized for synchronization and message passing, and a wide segment, designed for high-throughput bulk data transfers.

The wide segment is a scaled-up version of the narrow segment with 38 physical layers (PHYs) to increase bandwidth; its architecture is shown in Figure 3. The *protocol layer*, shown in Figure 3, arbitrates between AXI4 requests and responses and converts them to AXI4-Stream (AXIS) payloads. It handles the five independent channels of the AXI4 protocol (AW, AR, W, R, B) and applies backpressure to the AXI4 interface to prevent protocol-level deadlocks. Each AXIS payload includes a header that contains information about the packet type and credits required for flow control. The *data-link* layer further packetizes the payloads based on the available number of off-chip lanes; it also handles credit-based flow-control to ensure that no packets are lost, as well as synchronization and alignment of packets if multiple PHYs are configured. Additionally, the data-link layer features debugging capabilities, including a *Raw Mode* that allows the link to operate independently of the AXI4 interface by sending patterns over specific PHY channels for fault detection. Each PHY features an all-digital and source-synchronous interface with eight double-data-rate (DDR) lanes in each direction. On the transmitter side, the PHY operates with a forwarded

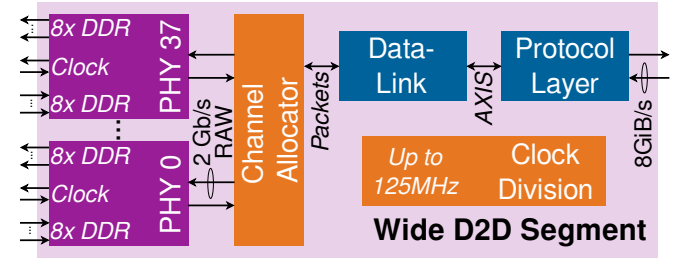


Fig. 3: Architecture of the wide D2D segment with its 38 source-synchronous double-data-rate PHYs, carrying up to 2 GiB/s of raw data at a clock speed of 125 MHz.

clock derived from the system clock. On the receiver side, the transmitted packets are synchronized with the system clock and reassembled into the original payload. The narrow and wide segments can achieve effective duplex bandwidths of up to 1.33 Gb/s and 64 Gb/s, respectively. The wide segment additionally features a *channel allocator* to enable fault tolerance. An initial calibration detects faulty PHYs, which can individually be disabled; the channel allocator then reshuffles packets among the functional PHYs with only linear bandwidth degradation. This fault tolerance mechanism ensures reliable communication across chiplets, even in the presence of manufacturing defects.

The Occamy chiplet relies on frequency-locked loops (FLLs) to generate on-chip clocks for each of its three clock domains: the *compute* domain, the *peripheral* domain, and the *HBM2E PHY* domain. The *compute* domain includes the compute groups, the 64-bit host, the chiplet-level interconnect, the D2D link, and the HBM2E controller. Like the groups, the D2D link and the HBM2E subsystem can be clock-gated through memory-mapped configuration registers.

III. PROGRAMMING MODEL

Occamy’s compute cores support the unprivileged 32-bit RISC-V ISA (RV32G) and can be programmed using RISC-V assembly, bare-metal C/C++, or a higher-level code generator, providing the full software agility of a general-purpose system. An extended LLVM 15 toolchain featuring assembly and intrinsics support for Occamy’s ISA extensions as well as specialized scheduling models and optimization passes allows programmers to write high-performance code targeting dense and sparse applications alike.

Occamy leverages explicit, tiled data movement to achieve near-ideal ($\geq 75\%$) FPU utilizations: while its SU-enhanced worker cores process local data tiles in SPM, the cluster DMA engines simultaneously transfer double-buffered tiles between the SPMs and global memory (e.g. HBM2E). This approach combines the benefits of memory- and interconnect-efficient, latency-tolerant bulk (~ 10 KiB) DMA transfers and of low-latency, fine-granular access provided to worker cores by the banked SPMs.

We will first elaborate on how worker cores achieve high cluster-level compute throughput on both dense and sparse applications through the use of SUs, and then discuss system-level data movement and tiling for full applications.

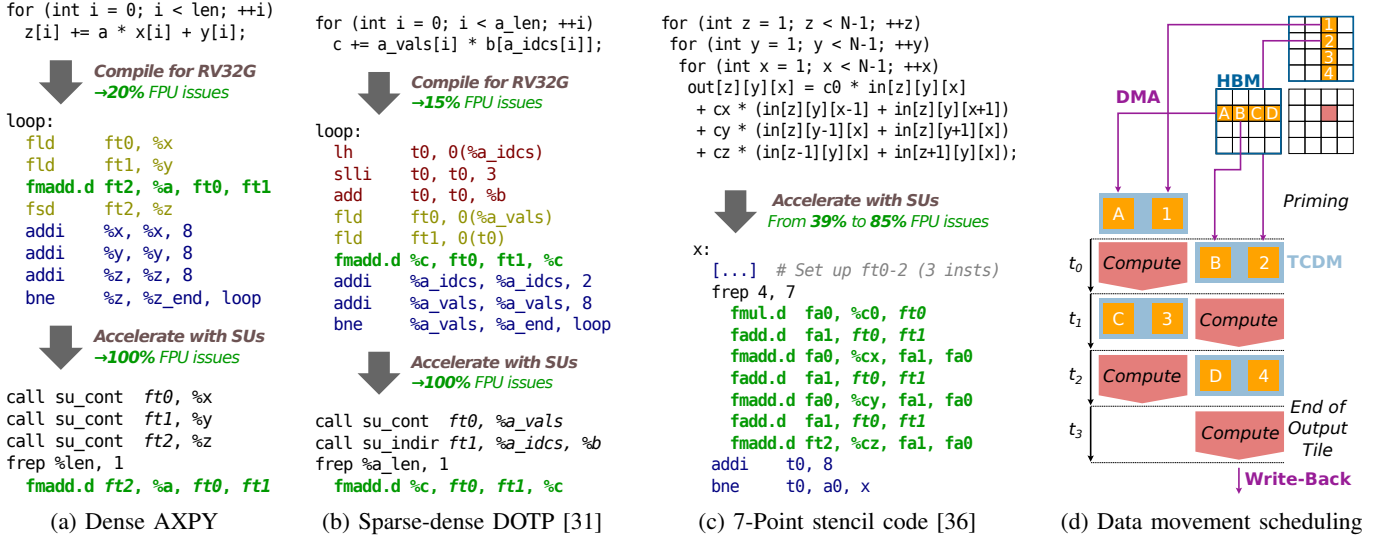


Fig. 4: (a-c) Example compute kernels and how they are accelerated on worker cores using SUs (green: useful compute, blue: iteration, orange: load-stores, red: indirection) and (d) high-level overview of data movement scheduling for tiled workloads.

A. SU Performance Benefits

Our SUs maximize FPU utilization on both dense and sparse workloads by eliminating the control overheads of streaming SPM accesses. They obviate address calculations and load-store issues, hide SPM access stalls, and enable multiple concurrent load-stores without a superscalar core. In this section, we demonstrate on three simple FP64 compute kernels (Figures 4a to 4c) how our SUs can be programmed to leverage the above benefits and enable the significant performance gains we later present in detail in Section V-B.

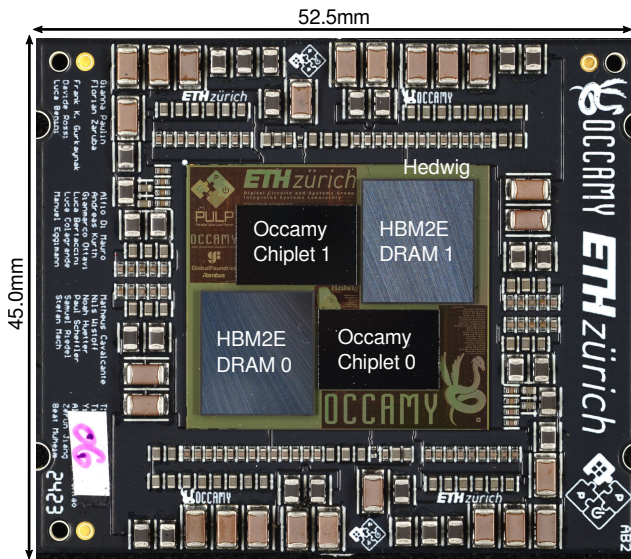
When compiled for the baseline RV32G ISA, the scaling vector sum (AXPY) in Figure 4a issues at most one useful FMA every eight cycles: three of the shown loop instructions perform load-stores (shown in orange) and another four handle iteration control (shown in blue), resulting in an eight-instruction loop in which only *one* instruction (the FMA `fmadd.d`) utilizes the FPU to perform useful compute. While code optimizations can further reduce iteration overheads, they cannot eliminate load-stores; even with a $4\times$ loop unroll, we observe an FPU issue fraction (and thus maximum FPU utilization) of only 20%. When accelerating this kernel with SUs, we eliminate all load-stores and address calculations by merging them into the register accesses of `fmadd.d`. Before entering the loop, we configure our three SUs, connected to the registers `ft0` to `ft2`, to continuously stream the operands `x` and `y` from SPM and the result `z` to SPM as shown. When the useful `fmadd.d` instruction accesses these registers, the SUs implicitly perform the associated address calculations and load-stores in hardware. Together with our FREP hardware loop, which eliminates the loop branch, the loop now consists only of the useful FMA instruction, which is issued repeatedly as shown. In practice, kernel setup overheads and SPM access contention prevent us from achieving 100% FPU utilization, but Occamy still reaches an average FPU utilization of 78% on dense LA workloads as we will show in Section V-B.

Figure 4b shows the code for a sparse-dense dot product.

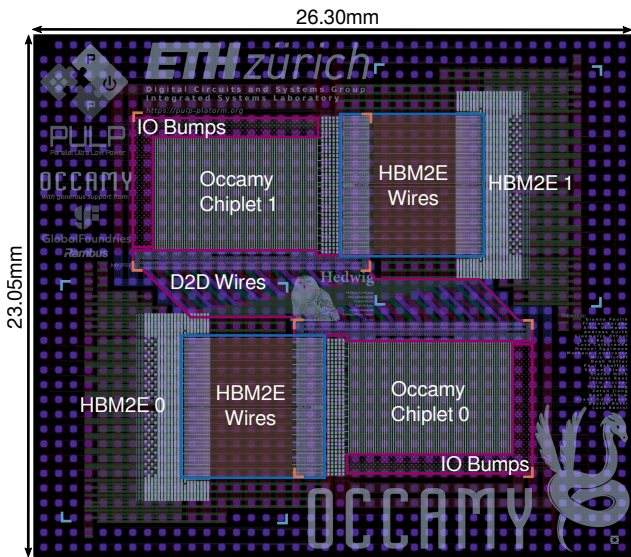
The sparse operand a is stored as two arrays, one holding nonzero values (`a_vals`) and another holding their positions (`a_idcs`). In addition to those seen in AXPY, the sparsity-induced *indirection* `b[a_idcs[i]]` incurs further address computation overheads on the baseline RV32G ISA (shown in red), limiting the fraction of useful FPU issues to 15% even with a $4\times$ loop unroll. Our SUs can accelerate this kernel by handling indirection fully in hardware: the SU of `ft1` is configured to fetch the indices `a_idcs` and use them to read from the dense vector `b`, yielding the values `b[a_idcs[i]]` when `ft1` is read. In parallel, the SU of `ft0` continuously reads the sparse values `a_vals`. By repeatedly issuing `fmadd.d` using FREP as shown, we can accumulate the partial products `a_vals[i]*b[a_idcs[i]]` without any non-compute instructions in the loop. The FPU utilization achieved in practice is no longer bound by control overheads, but by the SPM’s throughput and stream length imbalances [31].

Figure 4c shows one time iteration of a star-shaped stencil computation on a 3D grid. Stencils with complex shapes incur irregular memory access patterns, which are hard to optimize and prone to contention. Through predefined index arrays, our indirection-capable SUs can stream *arbitrary* SPM access sequences, eliminating the associated load-store and address calculation issues. In the example shown, we can store the offsets of all reads from the `in` grid relative to the center point `in[x][y][z]` in constant index arrays; our SUs can then repeatedly stream these index arrays with a different base address on each iteration of the innermost (`x`) loop. We can leverage this method, which is described in full detail in [36], to stream the data for *any* stencil code in ideal processing order. The method can also be combined with our FREP hardware loop for grid unrolling as shown. In our example, the SUs increase the fraction of FPU issues from 39% on an RV32G baseline to 85%.

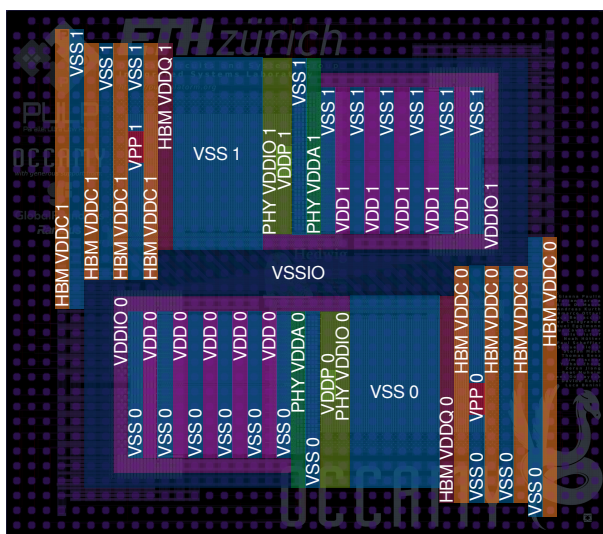
We re-emphasize that our SUs are *general-purpose* extensions; they can accelerate *any* data-driven workload involving



(a) 2.5D Occamy assembly mounted on carrier PCB.



(b) Layout of the Hedwig interposer.



(c) C4 bump map of the Hedwig interposer.

Fig. 5: Design of Hedwig interposer and carrier PCB.

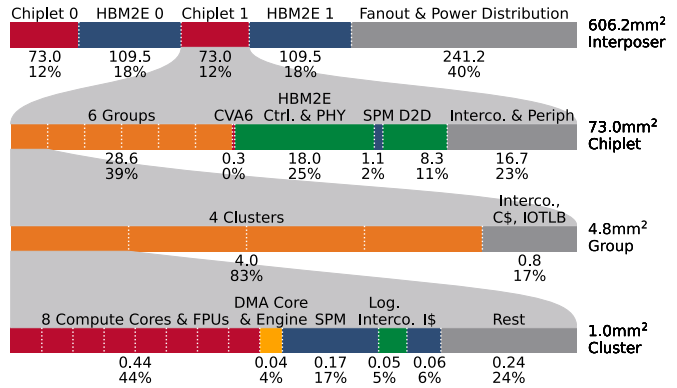


Fig. 6: Hierarchical area breakdown of the Occamy system.

$\leq 4D$ affine streams, indirect streams, tensor intersection, or union. Furthermore, while we focused on RISC-V assembly here to give precise insight into performance at the instruction level, SUs can be programmed entirely using the dedicated high-level (C/C++) compiler intrinsics we provide in our extended LLVM 15 toolchain.

B. DMA Engines and Data Movement

Occamy features a programmable DMA engine in each cluster to facilitate efficient data movement between the local SPMs, the HBM2E DRAM, and other clusters or chiplets. The DMA engine optimizes data transfer by managing asynchronous, double-buffered data tiles, ensuring data movement overlaps with computation to maximize resource utilization.

To implement double buffering, the DMA engine is programmed to fetch the next data tile into a secondary buffer while the worker cores process the current tile. Once the computation on the current tile is complete, the DMA engine swaps the buffers, making the new data immediately available for processing. The 128 KiB cluster SPMs can support tiles tens of KiB in size, which is sufficient to hide the typical access latencies in the hundreds of cycles that accesses to HBM2E or the other chiplet may incur.

Figure 4d illustrates our double-buffered tiling strategy. In the diagram, the *compute* blocks represent the phases where the worker cores process data, while the *DMA* blocks correspond to the data transfer phases where new tiles are being transferred into or out of the SPM.

IV. SILICON IMPLEMENTATION

The full Occamy 2.5D system was implemented and fabricated along with a dedicated carrier board, resulting in the compute module shown in Figure 5a. The 73 mm² chiplets were fabricated in GlobalFoundries' 12 nm LP+ FinFET node using a 13-metal stack. The two compute dies with their respective Micron *MT54A16G808A00AC-32* HBM2E stacks were mounted on *Hedwig*, a passive, 4-metal-stack 65 nm PKG-25SI interposer from GlobalFoundries, shown in Figure 5b.

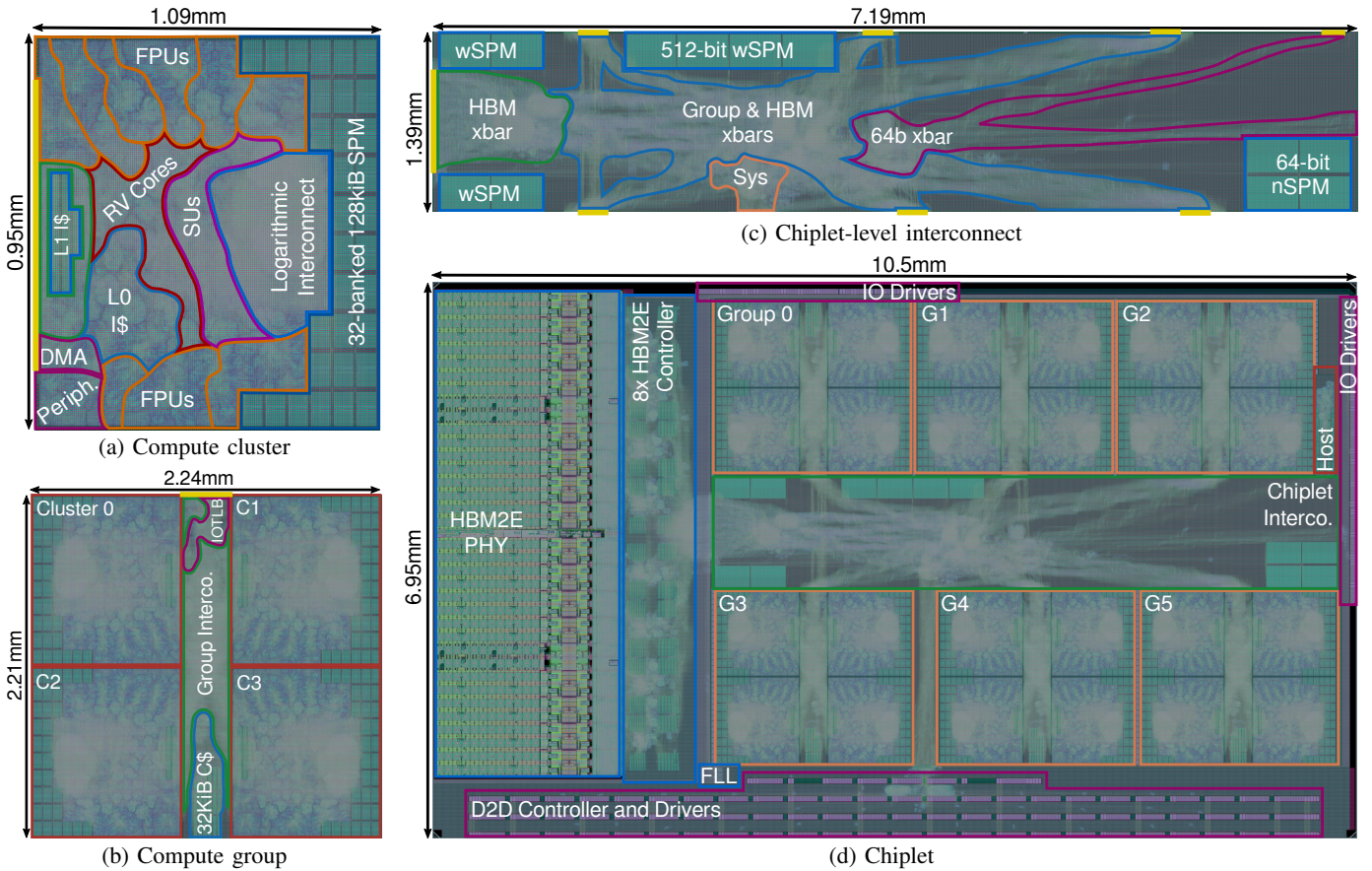


Fig. 7: Annotated physical layouts of the Occamy chiplet and its hierarchical components (block IO is shown in yellow).

A. Occamy Chiplets

The compute chiplets were synthesized, placed, and routed hierarchically using Synopsys’ *Fusion Compiler* 2022.3. We used 7.5-track standard cell libraries from Arm and HBM2E IPs (controller and PHY) provided by Rambus. We targeted a nominal compute domain clock of 1 GHz under typical conditions (0.8 V, 25 °C) with a worst-case constraint of 950 MHz. The peripheral domain was constrained to 500 MHz under worst-case conditions. The HBM2E controllers and PHY were constrained as specified to match the DRAM’s peak 3.2 Gb/s/pin throughput.

Figure 6 presents a hierarchical area breakdown of an entire Occamy assembly. Figure 7 shows the resulting hierarchical chiplet layout; we describe our implementation in a bottom-up fashion. In accordance with our findings in [37], we arranged the compute cluster’s IO ports and L1 instruction cache on one side and its SPM SRAMs in a U shape on the opposite side, resulting in the 1.0 mm² cluster layout shown in Figure 7a. The cluster is area-dominated by the nine RISC-V compute cores with extended FPU functionality (44%) and SPM (17%). The group layout, shown in Figure 7b, is almost entirely comprised of its four cluster macros (83%) and funnels its shared interconnect ports to a narrow interval on its north edge. The chiplet interconnect is shown in Figure 7c; the global SPM SRAMs were placed to avoid obstructing the shortest path for crossbar connections. Further, we implemented the

host processor, the eight HBM2E controllers, and the D2D link as hierarchical macros to simplify integration.

The top-level chiplet layout is shown in Figure 7d; it is area-dominated by the six compute groups (39%), HBM2E interface (25%), and D2D link (11%). In accordance with the interposer arrangement, the west and south chiplet beachfronts are fully reserved for the HBM2E and D2D interfaces, respectively, while the remaining off-interposer IO drivers are kept on the north and west edges. The central chiplet bumps are reserved for power delivery.

B. Hedwig Interposer

The Hedwig interposer is at the center of the 2.5D system, connecting the Occamy chiplets to each other, to their HBM2E stacks, and to the carrier board. On its top side, it exposes 45 μm -wide *microbump* openings accepting connections from the Occamy chiplets and HBM2E stacks through 15 μm -wide copper micropillars. On its bottom side, 1399 custom-designed hexagonal *C4 pads* with 320 μm openings and a 650 μm pitch allow us to solder the 2.5D assembly onto the carrier PCB using low-temperature bismuth-based *C4 bumps*.

The connections between the Occamy chiplets and HBM2E stacks were routed on the odd metal layers with a wire width of 2.5 μm and a pitch of 4.1 μm . The HBM2E wire length was kept below 4.9 mm, and ground shields were introduced on the even layers to ensure signal integrity. Figure 5b highlights the HBM2E wires; the routing density inside the rectangles

approaches 100%. The 39 D2D link channels were length-matched to 8.8 mm and combined into 24 wire bundles located at the center of Hedwig as shown in Figure 5b. The bundles were routed on the three upper metal layers in an alternating pattern, leaving the lowest layer for a shared ground connection. A routing width of $3.2\mu\text{m}$ with a pitch of $6.4\mu\text{m}$ was chosen.

The digital IO of the Occamy chiplets and HBM2E stacks was routed to Hedwig’s edge using $2.5\mu\text{m}$ traces on the three uppermost layers; placing IO-related C4 pads at the edge of Hedwig facilitates the fan-out to the carrier PCB. Figure 5c shows Hedwig’s C4 pad map, highlighting the IO-related connections as well as the sixteen power and three ground domains. The ground pads of IO drivers of the two chiplets are connected through the shielding of the D2D link, resulting in a shared IO ground *VSSIO*. For the rest of the power domains, each chiplet-HBM2E pair has its own ground *VSSx*. The compute fabric, host, and HBM2E controller on each chiplet are supplied through the core power net *VDDx*; the remaining power domains supply the HBM2E PHYs and memory stacks.

C. Carrier PCB

The carrier PCB completes the Occamy assembly at the lowest level. It serves three main purposes: giving the assembly mechanical stability, implementing the fan-out of the IO signals, and stabilizing the individual power domains. The 12-layer stack-up with $70\mu\text{m}$ -thick copper foil and *ROGERS RO4350B* high-stability, low-CTE laminate ensures high current delivery capabilities while providing sufficient mechanical strength. Decoupling capacitors are placed close to Hedwig on the carrier to comply with the power delivery requirements of the HBM2E stacks.

The carrier PCB implements an industry-standard *LGA 2011-3* CPU socket interface compatible with off-the-shelf mainboard sockets, facilitating the creation of application boards. Most of the 2011 pins are used for power and ground connections, with 877 exposed IOs. The carrier is designed to be strong enough to protect the fragile, $120\mu\text{m}$ -thick Hedwig interposer from mechanical stress while being placed into and removed from the test socket.

V. EXPERIMENTAL RESULTS

We create a custom testing infrastructure for Occamy as described in Section V-A to evaluate its compute performance and energy efficiency in Section V-B. We further evaluate Occamy’s performance and energy efficiency on ML inference applications in Section V-C. Finally, we evaluate the bandwidth scaling and energy efficiency of Occamy’s D2D link in Section V-D.

A. Silicon Measurement Setup

Figure 8a shows Occamy’s *bringup* board, which consists of a stack of two individual PCBs. The upper PCB holds an LGA 2011 zero insertion force (ZIF) socket for the Occamy system, connectors for the 16 power domains, an interface to

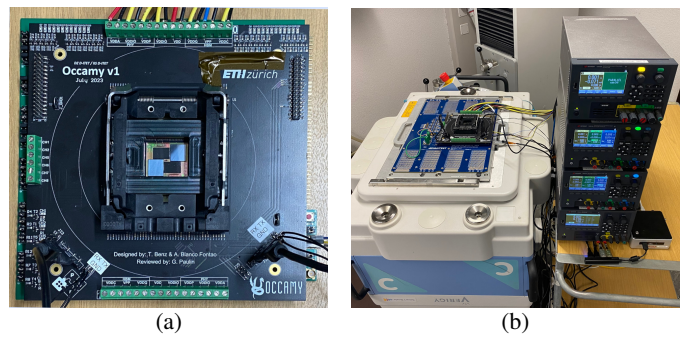


Fig. 8: (a) Bringup board enabling both testing on an V93000 ATE and standalone operation, and (b) measurement setup.

a *V93000* automatic test equipment (ATE) system, as well as JTAG, UART, and GPIO headers. For standalone operation, the lower PCB provides clocking resources, reset circuitry, configuration headers, and an SD card slot for each chiplet.

To evaluate Occamy, we connect the bringup board to an ATE system, ensuring a stable, low-jitter clock delivery. In all experiments, the temperature of the Occamy system is kept at 25°C through an active temperature forcing system. We use Keysight *E36200* series power supplies for power delivery and current measurements. Two Digilent *JTAG-HS2* programmers are used to program the Occamy system through JTAG, and two FTDI chips relay UART data to a testing workstation. We coordinate the power supplies, resets, programmers, and UART adapters through a dedicated Python script running on our testing workstation, which enables the automated, reproducible execution of applications on Occamy and the collection of current measurements across domains.

B. Compute Performance and Efficiency

Figure 9 summarizes Occamy’s performance and chiplet energy efficiency at the nominal 1 GHz compute clock on double-buffered dense and sparse FP64 compute workloads with and without SU acceleration. We use our ATE-based silicon measurement setup to determine execution times and chiplet power consumption at room temperature, repeating execution as necessary to allow for stable current measurements. Externally unobservable workload characteristics, such as the number of FLOPs or comparisons performed, are obtained analytically or through cycle-accurate simulation.

Figure 9a shows our results on FP64 dense LA workloads. Through affine streams, our SUs accelerate GEMM using 48^2 data tiles by 2.7 \times over baseline RV32G code, achieving a near-ideal FPU utilization of 89%, a performance of 686 GFLOP/s, and an energy efficiency of 39.8 GFLOP/s/W. On average, SU-accelerated dense workloads using the same 48^2 tile size achieve a somewhat lower FPU utilization of 78% as kernel and SU setup overheads become more pronounced and fewer FPU operations can be issued as fused (e.g. FMA) instructions. Nevertheless, SUs enable average speedups and energy efficiency improvements over RV32G of 2.4 \times and 1.5 \times , respectively.

Figure 9b shows our results on various FP64 stencil codes scaled out as described in [36], using 64^2 and 16^3 tiles for 2D

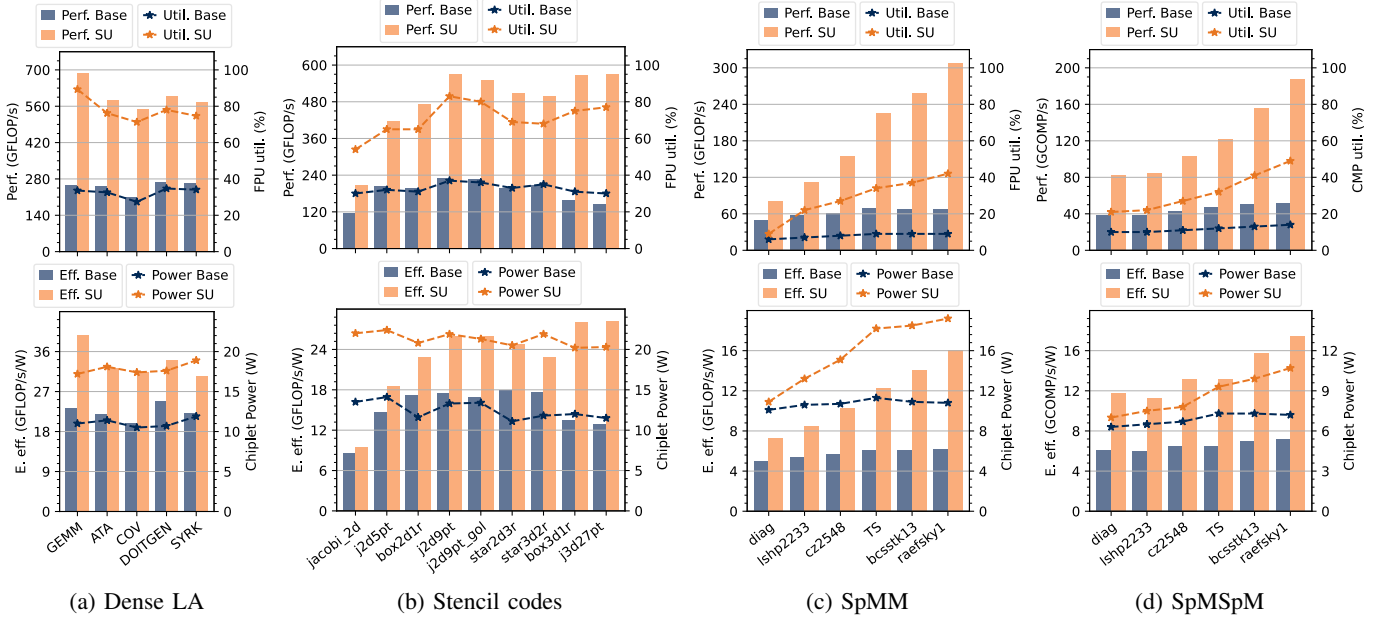


Fig. 9: Performance (top), energy efficiency, and power (bottom) for double-buffered FP64 workloads with and without SU acceleration. SpM(Sp)M left matrices (X axis) are real-world sparse matrices. SpMSpM right matrices are random with 1% density.

and 3D grids, respectively. Our indirect SUs accelerate all stencil codes by up to 3.9 \times compared to heavily optimized RV32G baseline code, achieving a peak FPU utilization of 83% and up to 571 GFLOP/s on the *j3d27pt* stencil. They also improve peak energy efficiency from 17.9 to 28.1 GFLOP/s/W. The remaining execution overheads preventing full FPU utilization with SUs are due to kernel initialization, SU setup, and SPM access contentions between worker cores.

Figures 9c and 9d show our results for sparse-dense (SpMM) and sparse-sparse matrix multiply (SpMSpM), respectively. In both cases, we multiply real-world left sparse matrices from [38] with random right matrices (1% density for SpMSpM); the left matrices are dynamically tiled and reused within compute groups. To demonstrate Occamy’s flexibility in handling sparse operands, the real-world left matrices are unstructured, cover different application domains, and span from 0.12% to 2.8% density (sorted left-to-right in figures). Through indirection, our SUs accelerate SpMM by up to 4.6 \times , achieving up to 307 GFLOP/s, 16.0 GFLOP/s/W, and 42% FPU utilization. We introduce index comparison rate as a figure of merit for sparse-sparse matrix computation performance; through index intersection, our SUs accelerate SpMSpM by up to 3.6 \times , reaching up to 187 GCOMP/s, 17.4 GCOMP/s/W, and index comparator utilizations of up to 49%. Normalizing our peak performance to the chiplet area dedicated to compute, we achieve up to 3.63 GCOMP/s/mm². For both SpMM and SpMSpM, performance improves with increasing left matrix density, which helps amortize SU setup costs as described in [31]. Accordingly, while Occamy maintains consistently high utilization as operands become denser, its performance and energy efficiency on extremely sparse operands eventually becomes limited by SU setup costs and the cluster SPMs’ finite indexing range.

Figure 10 shows how SU-accelerated GEMM performance

and energy efficiency scale as we reduce floating-point precision from 64 to 8 bits, leveraging our FPU’s SIMD capabilities. We consider FP16 GEMM without and with expanding FP32 accumulation (EXP suffix) and FP8 GEMM only with expanding FP16 accumulation. As we reduce precision, the achieved FPU utilization drops from 89% (FP64) to 66% (FP8 EXP). This is because the SIMD and mixed-precision kernels incur additional overheads: they must zero-initialize accumulators, reduce multiple accumulators packed in a 64-bit register, and possibly convert the higher-precision result to the original precision [30]. The FP64 kernel does not require conversions and avoids accumulator initialization through the non-accumulating `fmul.d` instruction in the first loop iteration. With these overheads in mind, the throughput and energy efficiency scale as expected; for FP8 GEMM with expanding accumulation, we achieve a throughput of 4.1 QP-TFLOP/s and an energy efficiency of 263 QP-GFLOP/s/W. On FP16, expanding GEMM is 6.5% more energy-efficient than non-expanding GEMM thanks to dedicated expanding dot product units in our FPU [30].

C. ML Inference Applications

We demonstrate Occamy’s architectural benefits on end-to-end applications by evaluating its performance and energy efficiency on two ML inference tasks: a GCN layer, which requires sparse-dense graph aggregation, and a full GPT-J large language model (LLM).

To evaluate GCNs, we implement the layer computation described in [39], which is used in classification tasks and involves both dense (feature recombination) and sparse-dense (graph aggregation) computation steps. We model the hidden layers of the GCN benchmarked in [40] on node classification, mapping an FP64 layer with 144 input and output features per

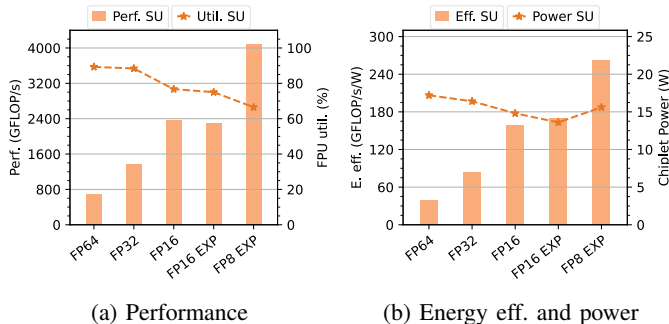


Fig. 10: Performance, energy efficiency, and power of GEMM at FP64 to FP8 precisions (EXP: expanding accumulation).

graph node across both chiplets. We double-buffer incoming features and distribute the layer’s output features among the 48 compute clusters. We measure Occamy’s performance and energy efficiency with and without SUs on the highly sparse citation graphs *webkb* [41], *cora* [42], and *citeseer* [42] with average node degrees of 1.8, 2.0, and 1.4, respectively.

Figure 11 shows the performance, energy efficiency, and power Occamy achieves on GCN layer computation, with the evaluated graphs sorted left-to-right by increasing node count. Our SUs enable an average speedup of 2.2 \times over an optimized RV32G baseline, raising the peak FPU utilization from 24% to 54% and achieving up to 413 DP-GFLOP/s or 8.01 DP-GFLOP/s/mm² on *citeseer*. Peak energy efficiency improves from 16.4 to 25.0 DP-GFLOP/s/W. As would be expected, our results fall between those achieved for dense and sparse workloads, showcasing Occamy’s ability to efficiently handle mixtures of sparse and dense compute. Overall, we observe a slight increase in SU performance and energy efficiency as graphs get larger, as this enables better amortization SU setup costs as was the case for SpMM.

We evaluate SU-accelerated LLM inference on Occamy by implementing a full FP16 GPT-J model. Building on the approach in [43], we hide communication overheads by staging input and intermediate data transfers concurrently with kernel execution. In the GPT-J blocks, both the layer normalization and linear layers are tiled to evenly distribute the workload across all clusters and maximize TCDM utilization. The attention mechanism is implemented using the *FlashAttention-2* [44] algorithm and fused with the subsequent concatenation and linear projection. Each chiplet produces half of the final *MHA* layer’s output matrix; the remaining computations, consisting of fused linear and layer normalization layers, are also tiled among the clusters as mentioned before.

Figure 12 shows the performance, energy efficiency, and power of Occamy running the full GPT-J model in non-autoregressive mode for sequence lengths from 128 to 1024 tokens. We use the standard measure of *token rate* (tok/s) to express LLM performance. At the shortest sequence length, our implementation achieves a peak throughput of 490 tok/s and an energy efficiency of 29.3 tok/s/W, achieving a peak FPU utilization of 75%. As can be seen in Figure 12a, increasing the sequence length leads to a gradual decrease in throughput, which is due to the well-understood quadratic

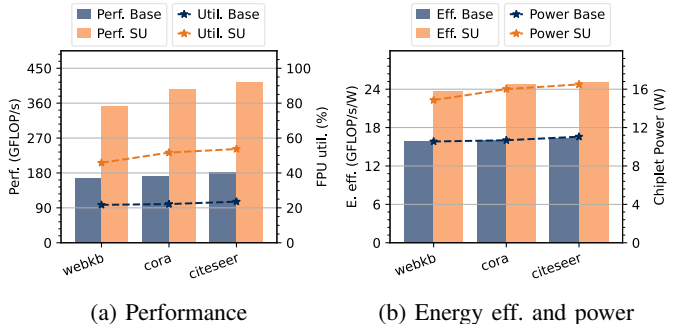


Fig. 11: Performance, energy efficiency, and power on GCN layer (144 \times 144, FP64) with and without SU acceleration.

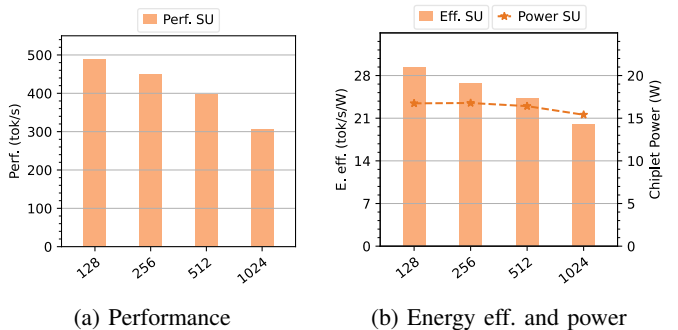


Fig. 12: Performance, energy efficiency, and power of SU-accelerated FP16 GPT-J LLM inference in non-autoregressive mode and for varying sequence lengths.

scaling of attention computation with sequence length. Accordingly, we see a gradual decrease in energy efficiency with increasing sequence length. While short sequences are dominated by matrix multiplication, as sequence length grows, more time is spent on the attention mechanism’s less efficient element-wise *softmax* operation.

D. Die-to-Die Link

Figure 13 shows the effective bandwidth of the wide D2D link under varying conditions analyzed in cycle-accurate RTL simulation. As expected, our bandwidth decreases linearly as we increase the number of disabled PHYs to mitigate faults. Furthermore, a high link utilization of 96% is achieved at a transfer size of 16 kB. We also determine the latency of communication between the two chips over the D2D link: accessing the other chiplet’s narrow SPM through the narrow segment from the host core incurs a latency of 27 cycles, while a DMA transfer over the wide segment experiences a latency of 61 cycles. On our silicon demonstrator, we measure the energy efficiency of the wide D2D segment to be 1.6 pJ/b.

VI. SoA REVIEW & COMPARISON

We will first review SoA hardware approaches to sparse compute acceleration, contrasting them with Occamy (Section VI-A), and then quantitatively compare Occamy’s performance and energy efficiency to those achieved on SoA, silicon-proven CPUs and GPUs (Section VI-B).

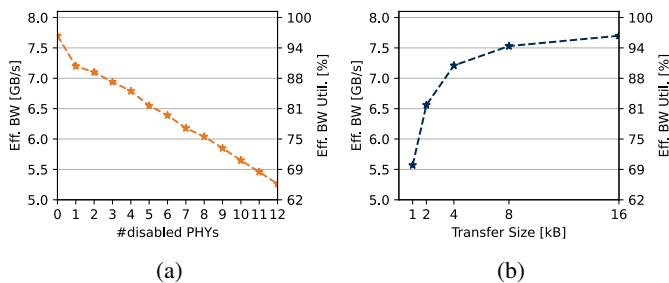


Fig. 13: (a) Linear effective bandwidth decrease for channel disabling on wide D2D segment and (b) effective bandwidth utilization for varying transfer sizes on wide D2D segment.

A. Sparse Hardware Acceleration SoA

Large-scale ML and HPC applications primarily target general-purpose CPUs and GPUs. These architectures efficiently handle dense compute [5], [6], but achieve low FPU utilization on sparse workloads ($\leq 10\%$ on sparse LA [6], [11], [12]) due to their data-dependent control flow and complex, indirect address computations.

To improve sparse compute efficiency, numerous accelerators have been proposed. Most notably, sparse ML accelerators achieving leading throughput and energy efficiency on ML inference tasks have been demonstrated in silicon [13]–[16]; however, they impose low-precision data formats (≤ 16 b) and low ($\leq 80\%$) or structured sparsity specific to ML workloads and are thus unsuitable for HPC. Generic sparse LA [17]–[20] or tensor algebra [21] accelerators are less domain-specific, with some demonstrated in silicon [19], [20], but most are still hardwired for specific LA operations [17]–[20] or dataflows [17], [18].

Discrete accelerators, while highly efficient, cannot match the flexibility and agility of general-purpose architectures. Recently, coarse-grained reconfigurable arrays (CGRAs) architectures have been proposed, supporting streaming indirection, intersection, and union in hardware [22], [23]. One such CGRA, *Onyx* [23], was recently demonstrated in silicon. However, CGRAs are still highly challenging to productively program [45], and *Onyx* only supports INT16 and BF16 data formats of insufficient precision for most HPC workloads.

Another common approach to maintain generality is through ISA extensions for CPUs and GPUs that accelerate sparse compute [24]–[29]; however, most of these extensions are not demonstrated in silicon [24]–[29] and only accelerate one- [24]–[27] or two-sided [28], [29] sparse operations. Thus, Occamy is the first silicon-proven general-purpose system to efficiently and comprehensively handle sparse workloads in 8-to-64-bit precisions.

B. Comparison to SoA CPUs & GPUs

Table I compares Occamy to SoA, silicon-proven GPUs and CPUs supporting the dominant ISAs (x86, Arm, RISC-V). To provide a holistic overview, we compare Occamy to both recently released processors (e.g. AMD Genoa, Nvidia H100), which usually lack published stencil and sparse-dense LA performance evaluations, as well as established processors

from prior generations (e.g. Fujitsu A64FX, Nvidia A100) whose real-world performance is well-studied and evaluated in literature. Occamy’s absolute performance is far ahead of other academic RISC-V silicon prototypes such as [46], achieving $8.3\times$ higher peak FP64 compute; it is much closer in peak throughput to the commercial Sophon SG2042 [47], [48] RISC-V manycore (0.77 vs 1.0 DP-GFLOP/s). Our D2D link, while comparatively low in throughput due to its simple PHY design, achieves a competitive energy efficiency 23% higher than that in AMD’s Rome [49]. Unlike other designs in Table I, Occamy’s entire digital compute architecture, including the groups, interconnect, host, and D2D link, is available as a free and open-source SystemVerilog RTL description.

On FP64 dense LA, Occamy’s SUs enable competitive FPU utilization through affine streams. Our 89% peak FPU utilization is notably higher than that achieved on AMD’s Rome [50] and Fujitsu’s A64FX [6] and is comparable to the 95% reached on Nvidia’s A100 GPU [5]. At up to 13.3 DP-GFLOP/s/mm², dense LA on Occamy is highly area-efficient: scaled to our 12 nm node, we achieve a higher compute density than all competitors except Schmidt et al. [46], A100, and H100 [51], [52]. Occamy’s peak dense LA energy efficiency of 39.8 DP-GFLOP/s/W is notably higher than that of the central processing units (CPUs) we compare to, but cannot reach the efficiency of Nvidia’s highly optimized A100 and H100 GPUs fabricated in more advanced nodes.

For FP64 stencil codes, Occamy’s indirect SUs enable significant utilization benefits over the compared CPU and GPU designs. Our 83% peak FPU utilization is $1.7\times$ higher than the leading 49% achieved on A100 [9] using CUDA compute only (to ensure a fair comparison, we normalized this FPU utilization to A100’s reduced 9.7 DP-TFLOP/s peak *excluding* tensor cores). While specialized transforms *can* leverage A100’s tensor cores to reach a higher peak throughput [53] (albeit at lower FPU utilization of 31%), the corresponding node-normalized compute density is still $1.2\times$ lower than the 11.1 DP-GFLOP/s/mm² Occamy achieves.

On sparse-dense FP64 LA, Occamy’s indirect SUs and explicitly managed memory hierarchy enable even higher utilization gains. Although all competitors have ISA-level support for scatter-gather, they reach at most 8.1% FPU utilization on AMD Rome [10], $5.2\times$ less than the 42% we achieve; this highlights the importance of our explicitly managed dataflow. We also achieve the highest technology-node-normalized compute density of 5.95 DP-GFLOP/s/mm², $11\times$ higher than the leading competitor A64FX [11]. While A100 introduces hardware support for 2:4 structured sparsity (≤ 2 nonzeros each block of four elements) [54], this feature cannot be used in [12] as it is specifically designed for deep learning on ≤ 32 b datatypes and ineffective in processing the highly sparse ($\geq 95\%$) data found in graph ML and HPC applications. As a result, A100’s inflexible GPU datapath achieves at most 2.9% FPU utilization, which is less than more agile CPU architectures we compare to.

To summarize, Occamy is the first 2.5D-integrated multi-chiplet RISC-V manycore demonstrated in silicon. Compared to state-of-the-art CPUs and GPUs, it achieves competitive FPU utilization (89%) on dense LA, as well as leading

TABLE I: Comparison of Occamy to SoA, silicon-proven GPUs and CPUs supporting the dominant ISAs (x86, Arm, and RISC-V).

		Schmidt et al. [46]	Sophon SG2042 [47]	AMD Rome [35], [55]	AMD Genoa [56], [57]	Fujitsu A64FX [58]	Nvidia A100 [59]	Nvidia H100 [51], [52]	Intel Sapphire Rapids [60], [61]	Occamy (Ours)
General	Assembly	Single Die	Single Die	Organic Substrate	Organic Substrate	2.5D Passive Interp.	2.5D CoWoS ^a	2.5D CoWoS ^a	2.5D EMIB ^b	2.5D Passive Interp.
	2.5D Compute Cfg.	-	-	8 Die	12 Die	1 Die	1 Die	1 Die	4 Die	2 Die
	2.5D DRAM Cfg.	-	-	1 IO Die	1 IO Die	4 HBM2	6 HBM2	5 HBM3	4 HBM2E	2 HBM2E
	Die Technology	16nm FinFET	12nm FinFET ^c	7nm FinFET	5nm FinFET	7nm FinFET	7nm FinFET	TSMC 4N FinFET	Intel 7 SuperFin	12nm FinFET ^d
	ISA	RV64GXhwacha4	RV64GCV (RVV v0.7.1)	x86-64, AVX2	x86-64, AVX-512	Armv8.2-A SVE ^e	PTX ISA, CC 8.0	PTX ISA, CC 9.0	x86-64, AVX-512, DL Boost, AMX	RV32GXoc ^{f,g}
	Open-Source RTL	Partially (Core)	Partially (Core) ^h	No	No	No	No	No	No	Partially (Compute)
	Freq. [GHz]	1.44	2.00	2.25 ^p	2.40 ^p	2.20	1.41	1.98	2.60	1.00
Voltage [V]	1.0	0.8	0.8	-	0.8	0.8	-	-	0.8	
Circ. Size	Transistors	0.5B	-	39B	78B ^t	8.8B	54B	80B	-	4.8B
	Die Area [mm ²]	24.0	585 ⁱ	592 ^k	840 ^k	420	826	814	1600	146
	Norm. Comp. Area [mm ²] ^l	3.86 (0.48/Core)	292 (4.6/Core)	442 (6.9/Core)	1183 (12.3/Core)	243 (5.1/Core)	632 (5.9/SM)	1170 (8.9/SM)	1024 (17/Core)	51.5 (1.0/Cluster)
RAM	System DRAM	-	≤256GiB DDR4	≤4TiB DDR4	≤6TiB DDR5	32GiB HBM2	40GiB HBM2	80GiB HBM3	≤4TiB DDR5	32GiB HBM2E
	On-Chip SRAM	4.5 MiB	64MiB L3\$	128MiB L3\$	384MiB L3\$	32MiB L2\$	40MiB L2\$	50MiB L2\$	64GiB HBM2E	9MiB SPM
D2D Link	Technology	-	-	IFOP ^m [35]	IFOP ^m [57]	-	-	-	EMIB ^b /MDFIO ⁿ [60]	Fully digital DDR
	#Links	-	-	8	12	-	-	-	20	38+1
	#Wires/Link	-	-	72	-	-	-	-	-	18
	R+W BW [GB/s]	-	-	440	1044	-	-	-	10000	16 ^o
	R+W BW/Link [GB/s]	-	-	55/Link	87/Link	-	-	-	500/Link	0.42/Link
E. Eff [pJ/bit]	-	-	2.0	-	-	-	-	0.5	1.6 ^o	
Peak Compute Throughp.	FP Formats	FP64/32/16	FP64/32/16	FP64/32	FP64/32	FP64/32/16	FP64/32/16	FP64/32/16/8	FP64/32/16/8	FP64/32/16/8
	[TFLOP/s]	0.092/0.18/0.37	1.00/2.00/4.00[48]	2.30 ^p /4.61 ^p	5.53 ^p /11.1 ^p	3.38/6.76/13.5	19.5 ^q /156 ^q /312 ^q	66.9^q/495^q/989^q/1979^q	2.85 ^r [62]/5.71/75.3/151[63]	0.77/1.54/3.07/6.14
	[GFLOP/s/mm ²]	20.9/41.8/83.7	3.42/6.84/13.7	8.22 ^p /16.4 ^p	11.8 ^p /23.6 ^p	21.9/43.9/87.8	48.6 ^q /389 ^q /777 ^q	172^q/1270^q/2541^q/5082^q	4.84/9.67/128/255	14.9/29.8/59.6/119
	[GFLOP/s/mm ²] ^l	23.9/47.7/95.4	3.42/6.84/13.7	5.21 ^p /10.4 ^p	4.67 ^p /9.35 ^p	13.9/27.9/55.7	30.8 ^q /247 ^q /493 ^q	57.2^q/423^q/845^q/1691^q	2.78/5.57/73.5/147	14.9/29.8/59.6/119
Best Dense LA FP64	[GFLOP/s]	87.5 ^s [46], [64]	-	1600 ^p [50]	4428 [65]	1978 ^u [6]	18500 [5]	33348^{x,y,z} [67] [68]	2696 [6]	686
	FPU util.	95% [64]	-	70% ^p [50]	80% [65]	72% ^u [6]	95% [5]	81% ^{x,y,z} [67]	95% [6]	89%
	[GFLOP/s/W]	20.0 ^s [46]	-	-	-	16.9 ^u [58]	41.4 ^{x,y} [66]	65.4^{x,y} [66]	-	39.8
	[GFLOP/s/mm ²]	19.9 ^s [46]	-	5.71 ^p [50]	9.43 [65]	12.8 ^u [6]	46.1 [5]	85.7^{x,y,z} [67]	4.57 [6]	13.3
[GFLOP/s/mm ²] ^l	22.7 ^s [46]	-	3.62 ^p [50]	3.74 [65]	8.15 ^u [6]	29.3 [5]	28.5 ^{x,y,z} [67]	2.63 [6]	13.3	
Best Stencil FP64	[GFLOP/s]	-	-	855 ^p [7]	-	323 ^u [8]	6063 [53]	-	-	571
	FPU util.	-	-	37% ^p [7]	-	11% ^u [8]	49% ^v [9]	-	-	83%
	[GFLOP/s/W]	-	-	-	-	-	-	-	-	28.1
	[GFLOP/s/mm ²]	-	-	3.05 ^p [7]	-	2.10 ^u [8]	15.1 [53]	-	-	11.1
[GFLOP/s/mm ²] ^l	-	-	1.93 ^p [7]	-	1.33 ^u [8]	9.58 [53]	-	-	11.1	
Best Sp-dense LA FP64	[GFLOP/s]	-	-	187 ^p [10]	67.5 [65]	131 ^u [11]	286 ^v [12]	-	198 [6]	307
	FPU util.	-	-	8.1% ^p [10]	1.2% [65]	4.7% ^u [11]	2.9% ^v [12]	-	6.9% [6]	42%
	[GFLOP/s/W]	-	-	-	-	-	-	-	-	16.0
	[GFLOP/s/mm ²]	-	-	0.67 ^p [10]	0.14 [65]	0.85 ^u [11]	0.71 ^v [12]	-	0.33 [6]	5.95
[GFLOP/s/mm ²] ^l	-	-	0.42 ^p [10]	0.06 [65]	0.54 ^u [11]	0.45 ^v [12]	-	0.19 [6]	5.95	

^a Chip on Wafer on Substrate ^b Embedded Multi-Die Interconnect Bridges ^c Based on core presented in [48] ^d Interposer: 65nm ^e 512 bit ^f Xoc := Xidma_Xsssr_Xminifloat ^g Host: RV64GC ^h RV64GC part of core as *OpenC910*
ⁱ Measured on released product ^k w/o IO die ^l Scaled to 12LP+ node using NAND2X1 gate areas (GE/μm²) or transistor density ^m Infinity-Fabric On-Package ⁿ Multi-Die Fabric I/O ^o Wide segment (38 links) ^p At base (non-boost) clock
^q Fully utilized tensor cores ^r At 2.6 GHz ^s At nominal 1V supply ^t Based on vector unit only ^u At below-peak clock (FPU util. relative to peak at reduced clock) ^v Tensor cores unused (FPU util. relative to peak without tensor cores)
^x Unknown whether tensor cores used ^y Based on many-GPU supercomputers ^z Based on "Virga" system using 448 H100 GPUs [68]

FPU utilizations (1.7 \times , 5.2 \times) and technology-node-normalized compute densities (1.2 \times , 11 \times) on stencil codes and sparse-dense LA, respectively. Unlike existing sparse compute accelerators and ISA extensions, our SUs are highly flexible and do not narrowly specialize to specific problem domains or data precisions. As such, Occamy combines high dense efficiency, sparse efficiency, and architectural flexibility in an unprecedented way.

VII. CONCLUSION

We presented Occamy, the first open-source silicon-proven 2.5D-integrated RISC-V manycore featuring 432 cores across two chiplets, 32 GiB of HBM2E DRAM, and a fully-digital fault-tolerant 1.6 pJ/b die-to-die (D2D) link. Occamy's compute cores feature an 8-to-64-bit SIMD-capable FPU kept busy by two ISA extensions: a hardware loop and three sparsity-capable streaming units (SUs). Our SUs enable high FPU utilization on both sparse and dense workloads through $\leq 4D$ affine and indirect streams as well as streaming intersection and union. Agile, latency-tolerant DMA engines copy large data tiles to and from local scratchpad memories (SPMs) to be processed by the compute cores with SUs.

We described the hierarchical implementation of our 12 nm FinFET compute chiplets and our 65 nm interposer *Hedwig*. On dense linear algebra (LA), Occamy achieves a competitive FPU utilization of up to 89% and an energy efficiency of up to 39.8 DP-GFLOP/s/W. On stencil codes, we reach an FPU utilization of up to 83% and a technology-node-normalized compute density of up to 11.1 DP-GFLOP/s/mm², improving by 1.7 \times and 1.2 \times , respectively, over SoA CPUs and GPUs. On sparse-dense LA, we achieve up to 42% FPU utilization and a technology-node-normalized compute density of up to 5.95 DP-GFLOP/s/mm², resulting in substantial gains of 5.2 \times and 11 \times over the SoA. We further achieve a sparse-sparse LA throughput of up to 187 GCOMP/s at 17.4 GCOMP/s/W, 3.63 GCOMP/s/mm², and a comparator utilization of 49%. Finally, we reach FPU utilizations of up to 75% and 54% on GPT-J inference and a GCN layer, respectively. The RTL description of Occamy's entire compute architecture is publicly available under a permissive open-source license².

ACKNOWLEDGMENTS

We thank the reviewers for their valuable feedback. We thank Florian Zaruba, Fabian Schuiki, Samuel Riedel, Alfio Di Mauro, Stefan Mach, Sina Arjmandpour, Noah Hütter, Andreas Kurth, Alfonso Fontao, Beat Muheim, Zerun Jiang, Georg Rutishauser, Silvio Scherr, Aldo Rossi, Cyril Koenig, Michael Rogenmoser, Cristian Cioflan, and Philippe Sauter for their invaluable contributions to this project. We are deeply grateful to GlobalFoundries, Avery, Micron, Rambus, and Synopsys for their generous support.

This work was supported in part through funding from the European High Performance Computing Joint Undertaking (JU) under Framework Partnership Agreement No 800928 and Specific Grant Agreement No: 101036168 (EPI SGA2) and No: 101034126 (The EU Pilot).

²<https://github.com/pulp-platform/occamy>

REFERENCES

- [1] T. Hoefer, D. Alistarh, T. Ben-Nun, N. Dryden, and A. Peste, "Sparsity in deep learning: Pruning and growth for efficient inference and training in neural networks," *J. Mach. Learn. Res.*, vol. 22, no. 1, pp. 10882–11005, 2021.
- [2] T. Dettmers, R. Svirfovski, V. Egiazarian, D. Kuznedelev, E. Frantar, S. Ashkboos, A. Borzunov, T. Hoefer, and D. Alistarh, "SpQR: A sparse-quantized representation for near-lossless LLM weight compression," in *12th Int. Conf. Learning Representations*, May 2024, accepted as poster.
- [3] H. Xia, Z. Zheng, Y. Li, D. Zhuang, Z. Zhou, X. Qiu, Y. Li, W. Lin, and S. L. Song, "Flash-LLM: Enabling cost-effective and highly-efficient large generative model inference with unstructured sparsity," *Proc. VLDB Endow.*, vol. 17, no. 2, pp. 211–224, 2023.
- [4] Z. Zhang, Y. Xu, J. Yang, X. Li, and D. Zhang, "A survey of sparse representation: Algorithms and applications," *IEEE Access*, vol. 3, pp. 490–530, 2015.
- [5] J. Kim, H. Kwon, J. Kang, J. Park, S. Lee, and J. Lee, "SnuHPL: high performance LINPACK for heterogeneous GPUs," in *Proc. 36th ACM Int. Conf. Supercomput.*, 2022, art. no. 18.
- [6] E. Siegmann, R. J. Harrison, D. Carlson, S. Chheda, A. Curtis, F. Coskun, R. Gonzalez, D. Wood, and N. A. Simakov, "First impressions of the Sapphire Rapids processor with HBM for scientific workloads," *SN Comput. Sci.*, vol. 5, 2024, art. no. 623.
- [7] L. Szustak, R. Wyrzykowski, L. Kuczynski, and T. Olas, "Architectural adaptation and performance-energy optimization for CFD application on AMD EPYC Rome," *IEEE Trans. Parallel Distrib. Syst.*, vol. 32, no. 12, pp. 2852–2866, 2021.
- [8] Y. Hirokawa, A. Yamada, S. Yamada, M. Noda, M. Uemoto, T. Boku, and K. Yabana, "Large-scale ab initio simulation of light-matter interaction at the atomic scale in Fugaku," *Int. J. High Perform. Comput. Appl.*, vol. 36, no. 2, pp. 182–197, 2022.
- [9] L. Zhang, M. Wahib, P. Chen, J. Meng, X. Wang, T. Endo, and S. Matsuoka, "Revisiting temporal blocking stencil optimizations," in *Proc. 37th ACM Int. Conf. Supercomput.*, 2023, pp. 251–263.
- [10] C. Alappat, G. Hager, O. Schenk, and G. Wellein, "Level-based blocking for sparse matrices: Sparse matrix-power-vector multiplication," *IEEE Trans. Parallel Distrib. Syst.*, vol. 34, no. 2, pp. 581–597, 2023.
- [11] C. Alappat, J. Laukemann, T. Gruber, G. Hager, G. Wellein, N. Meyer, and T. Wettig, "Performance modeling of streaming kernels and sparse matrix-vector multiplication on A64FX," in *Proc. IEEE/ACM Perform. Model., Benchmarking and Simul. of High Perform. Comput. Syst.*, 2020, pp. 1–7.
- [12] Y. Niu, Z. Lu, M. Dong, Z. Jin, W. Liu, and G. Tan, "TileSpMV: A tiled algorithm for sparse matrix-vector multiplication on GPUs," in *Proc. IEEE Int. Parallel Distrib. Process. Symp.*, 2021, pp. 68–78.
- [13] W.-C. Huang, I.-T. Lin, Y.-S. Lin, W.-C. Chen, L.-Y. Lin, N.-S. Chang, C.-P. Lin, C.-S. Chen, and C.-H. Yang, "A 25.1-TOPS/W sparsity-aware hybrid CNN-GCN deep learning SoC for mobile augmented reality," *IEEE J. Solid-State Circuits*, vol. 59, no. 11, pp. 3840–3852, 2024.
- [14] J. Yue, Y. Liu, X. Feng, Y. He, J. Wang, Z. Yuan, M. Zhan, J. Liu, J.-W. Su, Y.-L. Chung, P.-C. Wu, L.-Y. Hong, M.-F. Chang, N. Sun, C. Dou, X. Li, M. Liu, and H. Yang, "An energy-efficient computing-in-memory NN processor with set-associate blockwise sparsity and ping-pong weight update," *IEEE J. Solid-State Circuits*, vol. 59, no. 5, pp. 1612–1627, 2024.
- [15] X. Feng, W. Sun, C. Tang, X. Lin, J. Yue, H. Yang, and Y. Liu, "A 28-nm energy-efficient sparse neural network processor for point cloud applications using block-wise online neighbor searching," *IEEE J. Solid-State Circuits*, vol. 59, no. 9, pp. 3070–3081, 2024.
- [16] J.-F. Zhang, C.-E. Lee, C. Liu, Y. S. Shao, S. W. Keckler, and Z. Zhang, "SNAP: An efficient sparse neural acceleration processor for unstructured sparse deep neural network inference," *IEEE J. Solid-State Circuits*, vol. 56, no. 2, pp. 636–647, 2021.
- [17] N. Srivastava, H. Jin, J. Liu, D. H. Albonese, and Z. Zhang, "MatRaptor: A sparse-sparse matrix multiplication accelerator based on row-wise product," in *Proc. 53th Annu. IEEE/ACM Int. Symp. Microarchit.*, 2020, pp. 766–780.
- [18] S. Pal, J. Beaumont, D.-H. Park, A. Amarnath, S. Feng, C. Chakrabarti, H.-S. Kim, D. Blaauw, T. N. Mudge, and R. G. Dreslinski, "OuterSPACE: An outer product based sparse matrix multiplication accelerator," in *Proc. 2018 IEEE Int. Symp. High Perform. Comput. Archit.*, 2018, pp. 724–736.
- [19] D.-H. Park, S. Pal, S. Feng, P. Gao, J. Tan, A. Rovinski, S. Xie, C. Zhao, A. Amarnath, T. Wesley, J. Beaumont, K.-Y. Chen, C. Chakrabarti, M. B. Taylor, T. Mudge, D. Blaauw, H.-S. Kim, and R. G. Dreslinski, "A 7.3 M

- output non-zeros/J, 11.7 M output non-zeros/GB reconfigurable sparse matrix-matrix multiplication accelerator,” *IEEE J. Solid-State Circuits*, vol. 55, no. 4, pp. 933–944, 2020.
- [20] F. Sadi, J. Sweeney, T. M. Low, J. C. Hoe, L. T. Pileggi, and F. Franchetti, “Efficient SpMV operation for large and highly sparse matrices using scalable multi-way merge parallelization,” in *Proc. 52th Annu. IEEE/ACM Int. Symp. Microarchit.*, 2019, pp. 347–358.
- [21] K. Hegde, H. A. Moghaddam, M. Pellauer, N. C. Crago, A. Jaleel, E. Solomonik, J. S. Emer, and C. W. Fletcher, “ExTensor: An accelerator for sparse tensor algebra,” in *Proc. 52th Annu. IEEE/ACM Int. Symp. Microarchit.*, 2019, pp. 319–333.
- [22] V. Dadu, J. Weng, S. Liu, and T. Nowatzki, “Towards general purpose acceleration by exploiting common data-dependence forms,” in *Proc. 52th Annu. IEEE/ACM Int. Symp. Microarchit.*, 2019, pp. 924–939.
- [23] K. Koul, M. Strange, J. Melchert, A. Carsello, Y. Mei, O. Hsu, T. Kong, P.-H. Chen, H. Ke, K. Zhang, Q. Liu, G. Nyengele, A. Balasingam, J. Adivarahan, R. Sharma, Z. Xie, C. Torng, J. Emer, F. Kjolstad, M. Horowitz, and P. Raina, “Onyx: A 12nm 756 GOPS/W coarse-grained reconfigurable array for accelerating dense and sparse applications,” in *Proc. 2024 IEEE Symp. VLSI Technol. Circuits*, 2024, pp. 1–2.
- [24] M. Siracusa, V. Soria-Pardos, F. Sgherzi, J. Randall, D. J. Joseph, M. Moretó Planas, and A. Arnejach, “A tensor marshaling unit for sparse tensor algebra on general-purpose processors,” in *Proc. 56th Annu. IEEE/ACM Int. Symp. Microarchit.*, 2023, pp. 1332–1346.
- [25] J. M. Domingos, N. Neves, N. Roma, and P. Tomás, “Unlimited vector extension with data streaming support,” in *Proc. 2021 ACM/IEEE 48th Annu. Int. Symp. Comput. Archit.*, 2021, pp. 209–222.
- [26] M. Zhu, T. Zhang, Z. Gu, and Y. Xie, “Sparse tensor core: Algorithm and hardware co-design for vector-wise sparse neural networks on modern GPUs,” in *Proc. 52nd Annu. IEEE/ACM Int. Symp. Microarchit.*, 2019, pp. 359–371.
- [27] Z. Wang and T. Nowatzki, “Stream-based memory access specialization for general purpose processors,” in *Proc. 2019 ACM/IEEE 46th Annu. Int. Symp. Comput. Archit.*, 2019, pp. 736–749.
- [28] Y. Wang, C. Zhang, Z. Y. Xie, C. Guo, Y. Liu, and J. Leng, “Dual-side sparse tensor core,” in *Proc. 2021 ACM/IEEE 48th Annu. Int. Symp. Comput. Archit.*, 2021, pp. 1083–1095.
- [29] G. Rao, J. Chen, J. Yik, and X. Qian, “SparseCore: stream ISA and processor specialization for sparse computation,” in *Proc. 27th ACM Int. Conf. Architectural Support for Program. Lang. and Operating Sys.*, 2022, pp. 186–199.
- [30] L. Bertaccini, G. Paulin, M. Cavalcante, T. Fischer, S. Mach, and L. Benini, “MiniFloats on RISC-V cores: ISA extensions with mixed-precision short dot products,” *IEEE Trans. Emerg. Topics Comput.*, vol. 12, no. 4, pp. 1040–1055, 2024.
- [31] P. Scheffler, F. Zaruba, F. Schuiki, T. Hoefler, and L. Benini, “Sparse stream semantic registers: A lightweight ISA extension accelerating general sparse linear algebra,” *IEEE Trans. Parallel Distrib. Syst.*, vol. 34, no. 12, pp. 3147–3161, 2023.
- [32] T. Benz, M. Rogenmoser, P. Scheffler, S. Riedel, A. Ottaviano, A. Kurth, T. Hoefler, and L. Benini, “A high-performance, energy-efficient modular DMA engine architecture,” *IEEE Trans. Comput.*, vol. 73, no. 1, pp. 263–277, 2024.
- [33] G. Paulin, P. Scheffler, T. Benz, M. Cavalcante, T. Fischer, M. Eggimann, Y. Zhang, N. Wistoff, L. Bertaccini, L. Colagrande, G. Ottavi, F. K. Gürkaynak, D. Rossi, and L. Benini, “Occamy: A 432-core 28.1 DP-FLOP/s/W 83% FPU utilization dual-chiplet, dual-HBM2E RISC-V-based accelerator for stencil and sparse linear algebra computations with 8-to-64-bit floating-point support in 12nm FinFET,” in *Proc. 2024 IEEE Symp. VLSI Technol. Circuits*, 2024, pp. 1–2.
- [34] F. Zaruba, F. Schuiki, T. Hoefler, and L. Benini, “Snitch: A tiny pseudo dual-issue processor for area and energy efficient execution of floating-point intensive workloads,” *IEEE Trans. Comput.*, vol. 70, no. 11, pp. 1845–1860, 2020.
- [35] S. Naffziger, K. Lepak, M. Paraschou, and M. Subramony, “2.2 AMD chiplet architecture for high-performance server and desktop products,” in *Proc. 2020 IEEE Int. Solid-State Circuits Conf.*, vol. 63, 2020, pp. 44–45.
- [36] P. Scheffler, L. Colagrande, and L. Benini, “SARIS: Accelerating stencil computations on energy-efficient RISC-V compute clusters with indirect stream registers,” in *Proc. 61th ACM/IEEE Des. Automat. Conf.*, 2024, art. no. 251.
- [37] G. Paulin, M. Cavalcante, P. Scheffler, L. Bertaccini, Y. Zhang, F. Gürkaynak, and L. Benini, “Soft tiles: Capturing physical implementation flexibility for tightly-coupled parallel processing clusters,” in *Proc. 2022 IEEE Comput. Soc. Annu. Symp. on VLSI*, 2022, pp. 44–49.
- [38] T. A. Davis and Y. Hu, “The university of Florida sparse matrix collection,” *ACM Trans. Math. Softw.*, vol. 38, no. 1, 2011, art. no. 1.
- [39] T. N. Kipf and M. Welling, “Semi-supervised classification with graph convolutional networks,” in *5th Int. Conf. Learn. Representations*, April 2017, accepted as poster.
- [40] V. P. Dwivedi, C. K. Joshi, A. T. Luu, T. Laurent, Y. Bengio, and X. Bresson, “Benchmarking graph neural networks,” *J. Mach. Learn. Res.*, vol. 24, no. 1, Mar. 2024, art. no. 43.
- [41] Q. Lu and L. Getoor, “Link-based classification,” in *Proc. 20th Int. Conf. Mach. Learn.* AAAI, 2003, p. 496–503.
- [42] P. Sen, G. M. Namata, M. Bilgic, L. Getoor, B. Gallagher, and T. Eliassi-Rad, “Collective classification in network data,” *AI Magazine*, vol. 29, no. 3, pp. 93–106, 2008.
- [43] V. Potocnik, L. Colagrande, T. Fischer, L. Bertaccini, D. J. Pagliari, A. Burrello, and L. Benini, “Optimizing foundation model inference on a many-tiny-core open-source risc-v platform,” *IEEE Trans. Circuits Syst. Artif. Intell.*, vol. 1, no. 1, pp. 37–52, 2024.
- [44] T. Dao, “Flashattention-2: Faster attention with better parallelism and work partitioning,” in *12th Int. Conf. Learning Representations*, May 2024, accepted as poster.
- [45] L. Liu, J. Zhu, Z. Li, Y. Lu, Y. Deng, J. Han, S. Yin, and S. Wei, “A survey of coarse-grained reconfigurable architecture and design: Taxonomy, challenges, and applications,” *ACM Comput. Surv.*, vol. 52, no. 6, 2019, art. no. 118.
- [46] C. Schmidt, J. Wright, Z. Wang, E. Chang, A. Ou, W. Bae, S. Huang, V. Milovanović, A. Flynn, B. Richards, K. Asanović, E. Alon, and B. Nikolić, “An eight-core 1.44-GHz RISC-V vector processor in 16-nm FinFET,” *IEEE J. Solid-State Circuits*, vol. 57, no. 1, pp. 140–152, 2022.
- [47] C. Wei, “SG2042 technical reference manual,” 2023. [Online]. Available: <https://github.com/milkv-pioneer/pioneer-files/blob/650a5c5c/hardware/SG2042-TRM.pdf>
- [48] C. Chen, X. Xiang, C. Liu, Y. Shang, R. Guo, D. Liu, Y. Lu, Z. Hao, J. Luo, Z. Chen, C. Li, Y. Pu, J. Meng, X. Yan, Y. Xie, and X. Qi, “Xuantie-910: Innovating cloud and edge computing by RISC-V,” in *Proc. 2020 IEEE Hot Chips 32 Symp.*, 2020, pp. 1–19.
- [49] D. Suggs, D. Bouvier, M. Clark, K. Lepak, and M. Subramony, “AMD “ZEN 2”,” in *Proc. 2019 IEEE Hot Chips 31 Symp.*, 2019, pp. 1–24.
- [50] M. A. S. Bari, B. Chapman, A. Curtis, R. J. Harrison, E. Siegmann, N. A. Simakov, and M. D. Jones, “A64FX performance: experience on Oukami,” in *Proc. 2021 IEEE Int. Conf. Cluster Comput.*, 2021, pp. 711–718.
- [51] J. Choquette, “Nvidia Hopper GPU: Scaling performance,” in *Proc. 2022 IEEE Hot Chips 34 Symp.*, 2022, pp. 1–46.
- [52] Nvidia Corporation, “NVIDIA H100 tensor core GPU architecture,” 2024, v1.04. [Online]. Available: <https://resources.nvidia.com/en-us-tensor-core/gtc22-whitepaper-hopper>
- [53] Y. Chen, K. Li, Y. Wang, D. Bai, L. Wang, L. Ma, L. Yuan, Y. Zhang, T. Cao, and M. Yang, “ConvStencil: Transform stencil computation to matrix multiplication on tensor cores,” in *Proc. 29th ACM SIGPLAN Annu. Symp. Principles Practice Parallel Program.*, ser. PPOPP ’24. New York, NY, USA: Association for Computing Machinery, 2024, p. 333–347.
- [54] Nvidia Corporation, “NVIDIA A100 Tensor Core GPU Architecture,” 2020. [Online]. Available: <https://www.nvidia.com/content/dam/en-zz/Solutions/Data-Center/nvidia-ampere-architecture-whitepaper.pdf>
- [55] T. Singh, S. Rangarajan, D. John, R. Schreiber, S. Oliver, R. Seahra, and A. Schaefer, “2.1 Zen 2: The AMD 7nm energy-efficient high-performance x86-64 microprocessor core,” in *Proc. 2020 IEEE Int. Solid-State Circuits Conf.*, vol. 63, 2020, pp. 42–44.
- [56] B. Munger, K. Wilcox, J. Sniderman, C. Tung, B. Johnson, R. Schreiber, C. Henrion, K. Gillespie, T. Burd, H. Fair, D. Johnson, J. White, S. McLelland, S. Bakke, J. Olson, R. McCracken, M. Pickett, A. Horriuchi, H. Nguyen, and T. H. Jackson, ““Zen 4””: The AMD 5nm 5.7GHz x86-64 microprocessor core,” in *Proc. 2023 IEEE Int. Solid-State Circuits Conf.*, vol. 66, 2023, pp. 38–39.
- [57] R. Bhargava and K. Troester, “AMD next-generation “Zen 4” core and 4th gen AMD EPYC server CPUs,” *IEEE Micro*, vol. 44, no. 3, pp. 8–17, 2024.
- [58] S. Yamamura, Y. Akizuki, H. Sekiguchi, T. Maruyama, T. Sano, H. Miyazaki, and T. Yoshida, “A64FX: 52-core processor designed for the 442PetaFLOPS supercomputer Fugaku,” in *Proc. 2022 IEEE Int. Solid-State Circuits Conf.*, vol. 65, 2022, pp. 352–354.
- [59] J. Choquette, E. Lee, R. Krashinsky, V. Balan, and B. Khailany, “3.2 the A100 datacenter GPU and Ampere architecture,” in *Proc. 2021 IEEE Int. Solid-State Circuits Conf.*, vol. 64, 2021, pp. 48–50.

- [60] N. Nassif, A. O. Munch, C. L. Molnar, G. Pasdast, S. V. Lyer, Z. Yang, O. Mendoza, M. Huddart, S. Venkataraman, S. Kandula, R. Marom, A. M. Kern, B. Bowhill, D. R. Mulvihill, S. Nimmagadda, V. Kalidindi, J. Krause, M. M. Haq, R. Sharma, and K. Duda, "Sapphire Rapids: The next-generation Intel Xeon scalable processor," in *Proc. 2022 IEEE Int. Solid-State Circuits Conf.*, vol. 65, 2022, pp. 44–46.
- [61] A. Biswas, "Sapphire Rapids," in *Proc. 2021 IEEE Hot Chips 33 Symp.*, 2021, pp. 1–22.
- [62] Intel, "App metrics for intel microprocessors," 2024. [Online]. Available: <https://www.intel.com/content/dam/support/us/en/documents/processors/APP-for-Intel-Xeon-Processors.pdf>
- [63] —, "Architecture day 2021," 2021. [Online]. Available: <https://edc.intel.com/content/www/tw/zh/products/performance/benchmarks/architecture-day-2021/>
- [64] C. Schmidt, A. Ou, and K. Asanović, "Hwacha: A data-parallel RISC-V extension and implementation," in *Proc. Inaugural RISC-V Summit*, 2018, pp. 1–40.
- [65] AMD, "High Performance Computing Tuning Guide for AMD EPYC 9004 Series Processors," July 2024. [Online]. Available: https://www.amd.com/content/dam/amd/en/documents/epyc-technical-docs/tuning-guides/58002_amd-epyc-9004-tg-hpc.pdf
- [66] E. Strohmaier, J. Dongarra, H. Simon, and M. Meuer, "Green500 list," June 2024, 23rd edition. [Online]. Available: <https://www.top500.org/lists/green500/2024/06/>
- [67] —, "Top500 list," June 2024, 63rd edition. [Online]. Available: <https://www.top500.org/lists/top500/2024/06/>
- [68] C. Mellor, "Australia launches Virga cluster with Dell AI rackservers for health research," July 2024. [Online]. Available: <https://blocksandfiles.com/2024/07/03/australia-dell-based-virga-ai-workload-cluster/>



Paul Scheffler (Graduate Student Member, IEEE) received his B.Sc. and M.Sc. degrees in electrical engineering and information technology from ETH Zurich in 2018 and 2020, respectively. He is currently pursuing a Ph.D. degree in the Digital Circuits and Systems group of Prof. Benini. His research interests include hardware acceleration of sparse and irregular workloads, on-chip interconnects, many-core architectures, and high-performance computing.



Thomas Benz (Graduate Student Member, IEEE) received his B.Sc. and M.Sc. degrees in electrical engineering and information technology from ETH Zurich in 2018 and 2020, respectively. He is currently pursuing a Ph.D. degree in the Digital Circuits and Systems group of Prof. Benini. His research interests include energy-efficient high-performance computer architectures, memory interconnects, data movement, and the design of ASICs.



Viviane Potocnik (Graduate Student Member, IEEE) received her B.Sc. and M.Sc. degrees in electrical engineering and information technology from ETH Zurich in 2020 and 2022, respectively. She is currently pursuing a Ph.D. degree in the Digital Circuits and Systems group of Prof. Benini. Her research interests include heterogeneous architectures and the exploration of innovative data representation strategies to enhance the computational efficiency and adaptability on devices at the extreme edge.



Tim Fischer (Graduate Student Member, IEEE) received his B.Sc. and M.Sc. degrees in electrical engineering and information technology from ETH Zurich in 2018 and 2021, respectively. He is currently pursuing a Ph.D. degree in the Digital Circuits and Systems group of Prof. Benini. His research interests include scalable and energy-efficient on-chip and off-chip interconnects for high-performance computing.



Luca Colagrande (Graduate Student Member, IEEE) received his B.Sc. degree from Politecnico di Milano in 2018 and his M.Sc. degree from ETH Zurich in 2020. He is currently pursuing a Ph.D. degree in the Digital Circuits and Systems group of Prof. Benini. His research interests include energy-efficient general-purpose manycore accelerators and hardware-software co-design for machine learning and high-performance computing applications.



Nils Wistoff (Graduate Student Member, IEEE) received his B.Sc. and M.Sc. degrees from RWTH Aachen University in 2017 and 2020, respectively. He is currently pursuing a Ph.D. degree in the Digital Circuits and Systems group of Prof. Benini. His research interests include processor and system-on-chip design and secure computer architecture.



Yichao Zhang (Graduate Student Member, IEEE) received his B.Eng. degree from Heilongjiang University China in 2015 and his M.Sc. degree from Nanyang Technological University Singapore in 2017. He is currently pursuing a Ph.D. degree in the Digital Circuits and Systems group of Prof. Benini. His research interests include physically feasible manycore RISC-V architectures, parallel computing, and SIMD processing.



Luca Bertaccini (Graduate Student Member, IEEE) received his M.Sc. degree in Electronic Engineering from the University of Bologna in 2020. He is currently pursuing a Ph.D. degree in the Digital Circuits and Systems group of Prof. Benini. His research interests include heterogeneous systems-on-chip, energy-efficient hardware accelerators, computer arithmetic, and mixed-precision computing.



Gianmarco Ottavi received his M.Sc. degree from the University of Bologna in 2019. He has worked as a research fellow and is currently pursuing his Ph.D. at the Department of Electrical, Electronic, and Information Engineering "Guglielmo Marconi" at the University of Bologna. His research interests include energy-efficient architectures for DNN inference, vector machines, and computer architectures.



Frank K. Gürkaynak (Member, IEEE) has obtained his B.Sc. and M.Sc. in electrical engineering from the Istanbul Technical University, and his Ph.D. in electrical engineering from ETH Zürich in 2006. He is currently working as a senior scientist at the Integrated Systems Laboratory of ETH Zürich. His research interests include digital low-power design and cryptographic hardware.



Manuel Eggimann (Member, IEEE) received his B.Sc. and M.Sc. degrees in electrical engineering and information technology from ETH Zurich in 2016 and 2018, respectively. He completed his Ph.D. in the Digital Circuits and Systems group of Prof. Benini in 2023. His research interests include low-power hardware design, edge computing, and VLSI.



Davide Rossi (Senior Member, IEEE) received the Ph.D. degree from the University of Bologna, Bologna, Italy, in 2012. He has been a Post-Doctoral Researcher with the Department of Electrical, Electronic and Information Engineering "Guglielmo Marconi," University of Bologna, since 2015, where he is currently an Associate Professor. His research interests include energy-efficient digital architectures.



Matheus Cavalcante (Member, IEEE) received his M.Sc. degree in Integrated Electronic Systems from the Grenoble Institute of Technology (Phelma), France, in 2018. He completed his Ph.D. in the Digital Circuits and Systems group of Prof. Benini in 2023. His research interests include vector processing, high-performance computer architectures, and emerging VLSI technologies.



Luca Benini (Fellow, IEEE) holds the chair of Digital Circuits and Systems at ETH Zurich and is Full Professor at the Università di Bologna. Dr. Benini's research interests are in energy-efficient computing systems design, from embedded to high-performance. He has published more than 1000 peer-reviewed papers and five books. He is a Fellow of the ACM and a member of Academia Europaea.



Gianna Paulin (Member, IEEE) received her B.Sc. and M.Sc. degrees in electrical engineering and information technology from ETH Zurich in 2018 and 2021, respectively. She completed her Ph.D. in the Digital Circuits and Systems group of Prof. Benini in 2023. She worked on energy-efficient compute architectures accelerating neural networks and was involved in more than seven tape-outs. In March 2024, she joined Axelera AI, where she is developing the next generation of AI accelerators.